A resolved CFDEM method for the interaction between the fluid and the discontinuous solids with large movement

Jia Mao [a,b], Lanhao Zhao [a], Xunnan Liu [a], Eldad Avital [c]

a. College of Water Conservancy and Hydropower Engineering, Hohai University, Xikang Rd., Nanjing, 210098, China

b. Geotechnical Research Institute of Hohai University, Xikang Rd., Nanjing, 210098, China

c. School of Engineering & Materials Science, Queen Mary University of London, Mile End Rd., London E1 4NS, UK

Corresponding author

Lanhao Zhao

Address: College of Water Conservancy and Hydropower Engineering, Hohai University, Xikang Rd., Nanjing, 210098, China

Email: zhaolanhao@hhu.edu.cn

Telephone: +8613914733646

Abstract A novel resolved CFDEM method, which is a combination of the computational fluid dynamics and the discrete element method, is proposed for the simulation of the strong coupling between the fluid and the discontinuous solids with large movement. The fluid flow governed by the full Navier-Stokes equations is simulated using fixed grids based on the Eulerian framework, whereas the motion of the discontinuous solids is modeled by the discrete element method using the Lagrangian description. The key challenge, namely the representation of the moving interfaces between the fluid and the solids in different frameworks, is handled by the immersed boundary method. Meanwhile, the governing equations of the coupled system are solved by the partitioned method in an iterative way to achieve a strong coupling effect. The breakthrough of the proposed resolved CFDEM method lies in the calculation of the fluid flow in fixed grids with high resolution, along with an accurate simulation of the interaction between the fluid and the discontinuous solids with arbitrary shapes and large movement. The reliability and the accuracy of the new method are validated by calculating several well-known benchmark examples. Good agreements are achieved between the present and the known results.

Keywords: fluid-solid interaction, discontinuous solids, discrete element method, immersed boundary method, partitioned method

Abbreviations

FSI	Fluid-solid interaction
FSI-C	FSI problems between the fluid and the continuous solids
FSI-D	FSI problems between the fluid and the discontinuous solids
ALE	Arbitrary Lagrangian-Eulerian
FDM	Fictitious domain method
DPM	Discrete phase method
CFD	Computational fluid dynamics
DEM	Discrete element method
CFDEM	Combination of the CFD and the DEM
BCM	Body conformed method
IBM	Immersed boundary method
RCFDEM	Resolved CFDEM method
IB	Immersed boundary
VIV	Vortex-induced vibration
DKT	Drafting-kissing-tumbling

Nomenclature

$\boldsymbol{V}_C$	Velocity at the centroid of the solid *C*
$\boldsymbol{U}$	Fluid velocity at the centroid of the solid *C*
$\boldsymbol{F}_D$	Interaction force in the unresolved CFDEM method
C_D	Drag coefficient
ρ	Fluid density
d_p	Diameter of the particle
ε	Void fraction
χ	Parameter associated with the Reynolds number of the particle
m	Mass of the solid body
t	Time
$\boldsymbol{\delta}$	Translational displacement
$\boldsymbol{F}_e$	External force
$\boldsymbol{F}_c$	Contact force
$\boldsymbol{F}_f$	Force applied to the solids by the fluid
c	Damping coefficient
I_M	Moment of inertia tensor
$\boldsymbol{\theta}$	Angular displacement

$\boldsymbol{M}$	Total torques
$\boldsymbol{F}_{cn}$	Normal contact force
$\boldsymbol{F}_{ct}$	Tangential contact force
k_p	Penalty parameter
β_c	Contact body
β_t	Target body
$S_{\text{overlapping}}$	Boundary of the overlapping domain of β_c and β_t
$\boldsymbol{n}$	Outward unit vector of $S_{\text{overlapping}}$
φ_c	Potential function for the contact body
φ_t	Potential function for the target body
A	Area of the triangle
A_1, A_2, A_3	Area of each sub-triangle
k_t	Tangential stiffness coefficient
$\Delta\boldsymbol{\delta}_t$	Increment of the tangential displacement
$\boldsymbol{R}$	Transfer matrix
$\bar{\boldsymbol{F}}_{ct}$	Transferred tangential contact force
φ_μ	Maximum static frictional angle
$\boldsymbol{u}$	Velocity of the fluid field
p	Pressure of the fluid field
$\boldsymbol{f}_b$	Body force
$\boldsymbol{\tau}$	Viscous stress tensor
μ	Dynamic viscosity
$\boldsymbol{f}$	Extra body force
$\boldsymbol{V}^{n+1}$	Desired velocity at the immersed boundary point
$\boldsymbol{U}^{n+1}$	Interpolated velocity at the immersed boundary point
I	Interpolation function
D	Distribution function
$\phi(\boldsymbol{x})$	Physical quantity at the grid node $\boldsymbol{x}$

$\Phi(\boldsymbol{X}_i)$	Physical quantity at the immersed boundary point $\boldsymbol{X}_i$
ΔS_i	Discrete area of $\boldsymbol{X}_i$
δ	Discrete delta function
g_b	Collection of grid nodes on both sides of the immersed boundary
N_{IBP}	Number of the immersed boundary points
$\Delta\boldsymbol{u}^*$	Intermediate velocity increment
$\Delta\boldsymbol{u}^{**}$	Correction of the velocity increment
$\boldsymbol{u}^{*,K}$	Intermediate velocity
ε	Tolerance
$\|\cdot\|$	A kind of norms
$\boldsymbol{F}_f$	Force acted on the solids by the fluid
$\boldsymbol{F}_s$	Force acted on the fluid by the solids
S_s	Solid boundary
S_{out}	Boundary of the calculated domain
Ω	Domain bounded by S_s and S_{out}
Ω''	Domain inside S_s
$\boldsymbol{I}$	Unit tensor
Ω'	Sum of Ω and Ω''
Re	Reynolds number
U_∞	Far-field velocity
D	Cylinder diameter
C_L	Lift coefficient
St	Strouhal number
f_{req}	Vortex shedding frequency
F_D	Drag force
F_L	Lift force
U^*	Reduced velocity

f_N	Natural vibration frequency
k	Spring stiffness coefficient
m^*	Mass ratio
ξ	Damping ratio
D_x	Transverse distance
D_y	Longitudinal distance
D_r	Straightt-line distance

1 Introduction

Fluid-solid interaction (FSI) problems are encountered in various engineering fields, including constructional engineering [1], renewable engineering [2], biomedical engineering [3] and others. The FSI effects become significant when the mutual dependence between the influence and the response increases [4]. Considering the extensive existence and the noticeable influence of FSI effects, robust numerical FSI methods are in high demand.

Even though diverse criteria exist in dividing the FSI problems, FSI problems can be classified into two categories according to the continuity of the solid, (i) FSI problems between the fluid and the continuous solids (FSI-C) [5-7], (ii) FSI problems between the fluid and the discontinuous solids (FSI-D) [8-10]. The simulation methods are relatively mature for FSI-C problems with small motion of the solids [11]. Problems with large movement of the solids, though challenging, can be solved by various approaches, including the arbitrary Lagrangian-Eulerian (ALE) method [12,13], the overset mesh method [14], the fictitious domain method (FDM) [15,16] and etc.

However, it poses a great challenge to simulate the FSI-D problems, especially when arbitrary large movement of the discontinuous solids is considered [17,18]. Since all the discontinuous solid bodies are often immersed in the fluid, the surfaces of the solids, which are the fluid-solid interfaces, compose the boundaries of the fluid domain, as shown in Figure 1. The large movement of the solids leads to the drastic and arbitrary change of the fluid domain. Hence, the methods used to solve the FSI-C problems are not desirable or manageable. The application of the ALE method often leads to the severe distortion of the mesh when the movement of the fluid-solid interfaces is sudden and significant. The overset mesh method can deal with the large movement of the solids, while each sub-grid, which is covered by a solid body, is not allowed to interact with other sub-grids. Otherwise, the overlap and the interaction

between sub-grids make it difficult to implement this approach. Hence, the overset mesh method is restricted to the modelling of the interaction between the fluid and finite solid bodies without impact, for example, the sedimentation of a small number of particles in a channel [19] and the interaction between the propeller and the fluid [20].

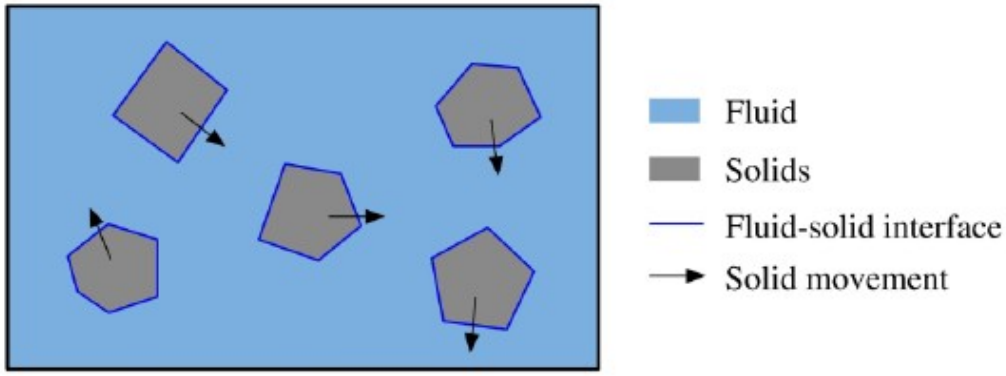

Figure 1 Sketch of the interaction between the fluid and the solids with large movement

Considering the complexity in simulating the moving solid boundaries, several Euler-Euler multi-phase models [21-23] have been proposed to avoid the direct description of the moving interfaces between fluid and solids. In these approaches, the dispersed solid bodies are treated as a continuum phase rather than being followed individually. A typical technique is modelling the solid phase with a non-Newtonian constitutive model. On this basis, the moving interfaces among different phases are treated as internal ones and captured by the level set method [24] or the volume of fluid method [25] implicitly. However, these methods are limited to model the problems which present fluidization characteristics, including the fluidized solids with high moisture and the debris flow, and the discontinuity and individual motion of the solids cannot be considered in the Euler-Euler multi-phase models. To account for the discontinuity property of the solids and track the trajectory, the discrete phase method (DPM) [26], which belongs to the Euler-Lagrange multi-phase models [27,28], has been proposed. Nevertheless, the interaction among the solids is neglected in the DPM and this model is only appropriate for dilute flows, where the dispersed second

phase occupies a low volume fraction, for example, the interaction between the gas and particles in a swirl burner [29]. The DPM cannot be employed if the volume fraction of the second phase is larger than 10%, such as in the simulation of the fluidized beds [30].

For the simulation of FSI-D problems with large movement of the solids, the optimal choice is combining the computational fluid dynamics (CFD) with the discontinuous methods, for instance, the discrete element method (DEM) [31]. A significant attempt is the establishment of the CFD-DEM (CFDEM) methods [32-35], in which the simulation of the coupling between the fluid and the discontinuous solids with arbitrary large movement is accomplished. However, the FSI force in the CFDEM methods is simplified as the drag force determined by the void fraction and the common empirical formulas were provided by Ergun [36] or Di Felice [37]. Essentially, the CFDEM methods, which can cope with the interaction among the solids, can be regarded as an improvement of the DPM. Nevertheless, the boundary conditions between the fluid and the solids are not set up accurately. The impact of each particle on the fluid is calculated independently by an empirical equation in the CFDEM methods. The influence of the wake flow on particles cannot be considered and the fluid field surrounding the particles is not precisely solved. Besides, the existing empirical equations are limited to the circular particles, rather than solid bodies with arbitrary shapes.

The unresolved CFDEM methods are the preferable choices when only the macroscopic behavior of the fluid and the solids is of interest [38]. However, the unresolved methods are incapable of simulating the FSI effect precisely. Therefore, it is important to develop an accurate simulation methodology for the kinetic characteristics of the solid bodies and the fluid by proposing a resolved CFDEM method. The key problem in establishing the resolved method is the description of the moving interfaces considering the arbitrariness of the body movement. Since the discontinuous solids are immersed in the fluid, the large movement of the solids makes the regeneration of the mesh in the body conformed method (BCM) complex

and difficult. To avoid the difficulty in regenerating the fluid mesh, an alternative choice is calculating the fluid flow and describing the moving fluid-solid interfaces based on the fixed grids in the Eulerian framework. The immersed boundary method (IBM) proposed creatively by Peskin [39] was used to model the blood flow in the heart with fixed mesh initially. Afterwards, the IBM has been extensively applied to solve the complicated solid boundaries immersed in the structured Eulerian grids for the fluid and present the force exerted to the fluid by the solids [40]. The innovation of the IBM is modelling the solid boundaries by adding a force term to the right-hand side of the Navier-Stokes momentum equation, which avoids the regeneration of the grids and decreases the calculation cost using the fixed mesh. The moving interfaces are represented by the immersed boundary points which are located on the solid boundaries.

In this paper, a resolved CFDEM method (RCFDEM) using the IBM is proposed to simulate the FSI phenomenon between the fluid and the discontinuous solids with large movement. In the RCFDEM method, the incompressible Navier-Stokes equations are applied as the governing equations for the fluid flow and the flow variables are solved according to the projection method based on the fixed mesh, while the DEM is used to simulate the movement of the solids. The IBM is applied to present the moving interfaces between the fluid and the solid bodies and calculate the FSI forces. The partitioned method is selected to solve the coupled system. Thereafter, several iterations are carried out to establish a strong coupling between the fluid and the solids, i.e., the stress balance and the movement compatibility. Specifically, the velocities of the solids are used as the boundary condition for the calculation of the fluid phase. Then, the achieved FSI force is employed as the boundary condition for the calculation of solids. A loop is adopted till the relevant convergence conditions are satisfied. In the above partitioned way, the convergence and the stability of the proposed RCFDEM method is improved significantly.

This paper is arranged as follows. The methodology is clarified in detail in Section 2, including the governing equations for solid bodies and the fluid, the

calculation of the interaction force and the iterative scheme for the coupled system. In Section 3, the accuracy of the proposed RCFDEM method is verified by four benchmark tests and then this method is employed to simulate the sedimentation of rigid bodies with arbitrary shapes. At the end of this paper, the conclusions are given.

2 Methodology

2.1 Overall view of the proposed RCFDEM method against the unresolved CDFEM approaches

In the FSI-D problems, the system for the fluid and the solids are coupled accurately by imposing adequate boundary conditions to the solid surfaces, i.e., the fluid-solid interfaces. Hence, the description of the solid boundaries with large movement plays an important role in numerical simulations. In the unresolved CFDEM method, an empirical equation has to be employed to estimate the fluid-solid interaction force and the sketch used to obtain the force is presented in Figure 2. The centroid of the solid is defined as *C* and the velocity is $\boldsymbol{V}_C$. The fluid velocity at Point *C* is marked as $\boldsymbol{U}$ which can be interpolated by the surrounding mesh nodes 1 to 4. The interaction force $\boldsymbol{F}_D$ is then obtained according to the difference between $\boldsymbol{V}_C$ and $\boldsymbol{U}$. For example, the empirical equation proposed by Di Felice [37] is

$$\boldsymbol{F}_D = \frac{1}{8} C_D \rho \pi d_p^2 (\boldsymbol{U} - \boldsymbol{V}_C) \left| \boldsymbol{U} - \boldsymbol{V}_C \right| \varepsilon^{1-\chi} \quad (11)$$

where C_D is the coefficient of the drag force, ρ is the fluid density, d_p is the diameter of the particle, ε is the void fraction, χ is a parameter associated with the Reynolds number of the particle. The explicit solution of the moving interfaces is

avoided in the unresolved method, while several inherent drawbacks still exist as follows.

(1) The empirical equation is limited to the circular particles. To the best knowledge of the authors, the existing empirical formulations are restricted to the circular solid bodies. In practical FSI-D problems, the shape of the solids is arbitrary.

(2) The influence of the solids on the fluid cannot be reflected accurately. The empirical equations are proposed to calculate the interaction force between the fluid and only one circular particle. Hence, the effects of each solid body on the fluid is considered separately based on Eq. Error: Reference source not found. However, the sum of the drag forces cannot represent the FSI effect precisely since the influences of different particles to the fluid are interrelated.

(3) The fluid-solid interfaces are not represented. The FSI forces calculated according to Eq. Error: Reference source not found are simplified to the centers of the corresponding particles. The fluid-solid interfaces, i.e., the solid surfaces, are not represented in the unresolved CFDEM method. Hence, the fluid cannot feel the existence of the particles and the resolution of the fluid is low.

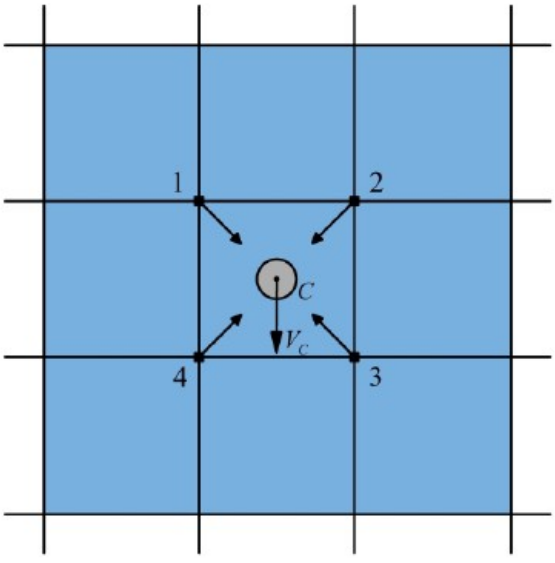

Figure 2 Sketch of the unresolved CFDEM method

Compared with the unresolved CFDEM method, the proposed RCFDEM method

calculates the fluid flow with high resolution and describes the fluid-solid interfaces accurately. The fluid and the solids are discretized in the Eulerian and Lagrangian framework respectively, and the solids are immersed in the fixed fluid mesh, as shown in Figure 3. To describe the solid with large movement and combine different frameworks, the IBM is employed in the resolved method and several immersed boundary points are allocated on each solid boundary. The velocity and the position of each immersed boundary point are determined by the discontinuous solid bodies. Extra body forces are acted on the nodes of the fluid mesh to satisfy the boundary conditions on the immersed boundary points and the kinematics of the fluid flow can be calculated. Subsequently, the reactive forces are applied to the solids. For this coupled system, an iteration should be pursued till a convergence is achieved. The fluid-solid coupled interaction can be manifested precisely when the boundary conditions on the immersed boundary points are satisfied.

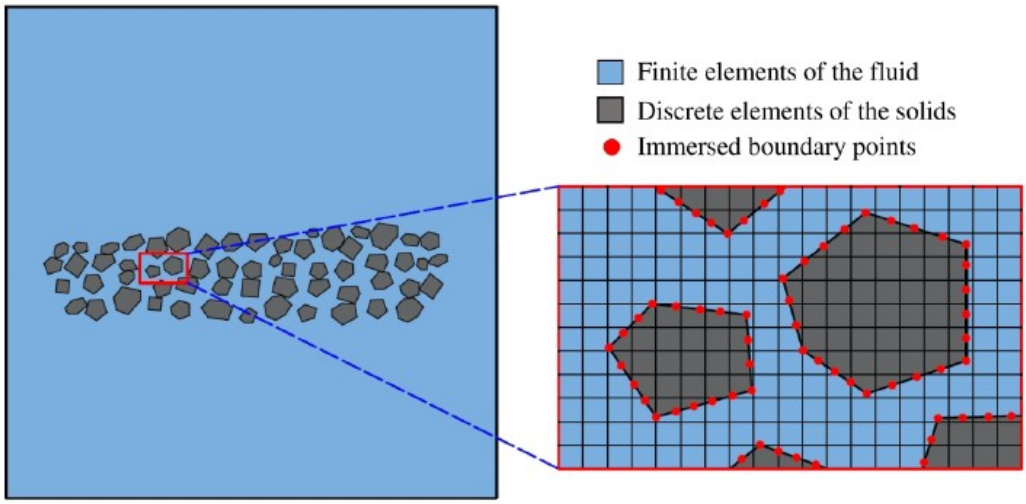

Figure 3 Sketch of the proposed RCFDEM method

The main characteristics of the RCFDEM method are as follows. The solid motion is described by the DEM, while the fluid flow is governed by the NSEs. The moving interfaces between the fluid and the solids and the interaction forces are simulated by the IBM. In order to achieve the strong coupling between the two systems, the governing equations are solved by the partitioned method in an iterative

way. In the following part of this section, the implementation of the RCFDEM method is illustrated in detail.

2.2 Governing equations for the solids

The movement of solid bodies is governed by the Newton's second law which takes the influence of the fluid into consideration. The governing equation can be written as

22* MERGEFORMAT ()

$$m\frac{d^2\boldsymbol{\delta}}{dt^2}=\boldsymbol{F}$$

33* MERGEFORMAT ()

$$I_M\frac{d^2\boldsymbol{\theta}}{dt^2}=\boldsymbol{M}$$

where m is the mass of the solid body, t represents time, $\boldsymbol{\delta}$ represents the translational displacement, $\boldsymbol{F}$ satisfies $\boldsymbol{F}=\boldsymbol{F}_e+\boldsymbol{F}_c+\boldsymbol{F}_f-c\frac{d\boldsymbol{\delta}}{dt}$, in which $\boldsymbol{F}_e$ is the external force, $\boldsymbol{F}_c$ is the contact force, $\boldsymbol{F}_f$ stands for the force applied to the solids by the fluid and c is the damping coefficient. I_M is the moment of inertia tensor, $\boldsymbol{\theta}$ is the angular displacement and $\boldsymbol{M}$ is the total torques, including the contributions of the external force, the fluid-solid interaction force and etc.

The term $\boldsymbol{F}_c$ is composed of the normal contact force $\boldsymbol{F}_{cn}$ and the tangential one $\boldsymbol{F}_{ct}$. The normal contact force $\boldsymbol{F}_{cn}$ is calculated as follows

44* MERGEFORMAT ()

$$\boldsymbol{F}_{cn}=k_p\int_{S_{\text{overlapping}}}\boldsymbol{n}(\varphi_c-\varphi_t)\,dS$$

where k_p is the penalty parameter, β_c is the contact body, β_t is the target body, $\boldsymbol{n}$ is the outward unit vector of $S_{\text{overlapping}}$ which is the boundary of the overlapping domain of β_c and β_t, φ_c and φ_t are the potential functions for the contact and target bodies according to the definition provided by Munjiza [41]. As shown in Figure 4, the potential function at an arbitrary point P in a triangle is defined as $\varphi(P) = \min\left(\frac{3A_1}{A}, \frac{3A_2}{A}, \frac{3A_3}{A}\right)$, where A represents the area of the triangle, A_1, A_2, A_3 represent the area of each sub-triangle.

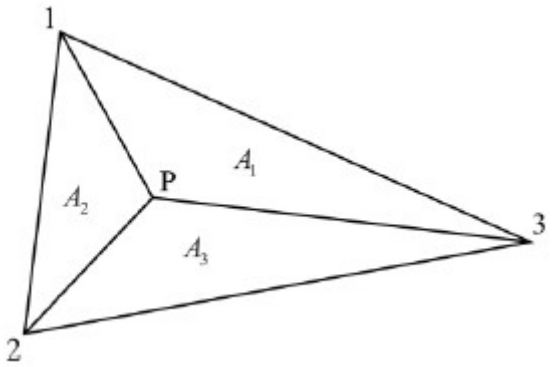

Figure 4 Sketch of the definition of the potential function

To calculate the tangential contact force $\boldsymbol{F}_{ct}$, the force-displacement law is applied. The detailed procedure is

Step 1: calculate the increment of the tangential contact force $\Delta\boldsymbol{F}_{ct}^{i}$

55* MERGEFORMAT ()

$$\Delta\boldsymbol{F}_{ct}^{i} = k_t \cdot \Delta\boldsymbol{\delta}_t^{i}$$

where k_t is the tangential stiffness coefficient, $\Delta\boldsymbol{\delta}_t^{i}$ is the increment of the tangential displacement at the i^{th} time step.

Step 2: transfer the direction of the tangential contact force in the previous time step $\boldsymbol{F}_{ct}^{i-1}$ to the direction of $\boldsymbol{F}_{ct}^{i}$ equivalently using the transfer matrix $\boldsymbol{R}$

66*
MERG
EFOR
MAT ()

$$\bar{\boldsymbol{F}}_{ct}^{i-1} = \boldsymbol{R}\boldsymbol{F}_{ct}^{i-1}$$

Step 3: calculate the current tangential contact force $\boldsymbol{F}_{ct}^{i}$

77*
MERG
EFOR
MAT ()

$$\bar{\boldsymbol{F}}_{ct}^{i\prime} = \bar{\boldsymbol{F}}_{ct}^{i-1} + \Delta\boldsymbol{F}_{ct}^{i}$$

88*
MERG
EFOR
MAT ()

$$\boldsymbol{F}_{ct}^{i} = \max\left(\bar{\boldsymbol{F}}_{ct}^{i\prime}, \boldsymbol{F}_{cn}^{i} \tan\varphi_{\mu} \right)$$

where φ_{μ} is the maximum static frictional angle.

2.3 Governing equations for the fluid

The fluid flow is governed by the full Navier-Stokes equations. Since the fluid-solid interaction should be considered, the direct-forcing IBM [42] is employed and an additional term is added to the right-hand side of the momentum equation. The governing equations including the extra body force for the incompressible flow are written as

99*
MERG
EFOR
MAT ()

$$\nabla\cdot\boldsymbol{u} = 0$$

1010*
MERG
EFOR

$$\frac{\partial\boldsymbol{u}}{\partial t} + \nabla\cdot(\boldsymbol{u}\boldsymbol{u}) = -\frac{1}{\rho}\nabla p + \frac{1}{\rho}\nabla\cdot\boldsymbol{\tau} + \boldsymbol{f}_{b} + \boldsymbol{f}$$

MAT ()

where $\boldsymbol{u}$ represents the velocity, t is time, p is the pressure, ρ is the density, $\boldsymbol{f}_b$ is the body force, $\boldsymbol{\tau}$ is the viscous stress tensor which satisfies $\boldsymbol{\tau} = \mu(\nabla \boldsymbol{u} + \nabla^T \boldsymbol{u})$, μ is the dynamic viscosity, $\boldsymbol{f}$ is an extra body force per mass unit exerted on the fixed grid. The extra body force term can be obtained according to the boundary condition of the direct-forcing IBM, i.e., the desired velocity at the immersed boundary point $\boldsymbol{V}^{n+1}$ equals to the interpolated velocity at the same point $\boldsymbol{U}^{n+1}$.

To calculate the term $\boldsymbol{f}$ in Eq. Error: Reference source not found, the interpolation function I and the distribution function D are defined. The function I is used to interpolate the physical quantities at grid nodes to immersed boundary points and the function D is applied to distribute the physical quantities at immersed boundary points to the grid nodes. The application of the above two functions are as follows

1111*

$$\Phi(\boldsymbol{X}_i) = I(\phi, \boldsymbol{X}_i) = \sum_{x \in g_b} \phi(\boldsymbol{x}) \delta(\boldsymbol{x} - \boldsymbol{X}_i)$$

MERG

EFOR

MAT ()

1212*

$$\phi(\boldsymbol{x}) = D(\Phi, \boldsymbol{x}) = \sum_{i=1}^{N_{\mathrm{IBP}}} \Phi(\boldsymbol{X}_i) \delta(\boldsymbol{x} - \boldsymbol{X}_i) \Delta S_i$$

MERG

EFOR

MAT ()

where $\phi(\boldsymbol{x})$ is the physical quantity, including $\boldsymbol{u}$, p, $\boldsymbol{f}$, at the grid node $\boldsymbol{x}$, $\Phi(\boldsymbol{X}_i)$ is the physical quantity at the immersed boundary point $\boldsymbol{X}_i$, ΔS_i is the discrete area of $\boldsymbol{X}_i$, δ is the discrete delta function, g_b is the collection of the grid nodes on both sides of the immersed boundary, N_{IBP} is the number of the immersed boundary points. g_b and N_{IBP} are determined according to the dependence domain of the functions I and D, respectively.

In consideration of the coupling between $\boldsymbol{u}$ and p, the governing equations for

the fluid are solved based on the Characteristic-based Split scheme [43]. The temporal-discretized formulation of Eq. Error: Reference source not found is

1313* MERGEFORMAT ()

$$\Delta \boldsymbol{u} = \boldsymbol{K}^{n} + \boldsymbol{R}^{n+1} + \boldsymbol{f}^{n+1}\Delta t$$

where the superscripts stand for the time step and the expressions for $\boldsymbol{K}^{n}$ and $\boldsymbol{R}^{n+1}$ are as follow

1414* MERGEFORMAT ()

$$\boldsymbol{K}^{n} = -\Delta t\left(\nabla\cdot(\boldsymbol{uu}) - \nabla\cdot\frac{\boldsymbol{\tau}}{\rho}\right) + \frac{\Delta t^{2}}{2}\boldsymbol{u}\cdot\nabla\left(\nabla\cdot(\boldsymbol{uu})\right)$$

1515* MERGEFORMAT ()

$$\boldsymbol{R}^{n+1} = -\Delta t\left(\frac{1}{\rho}\nabla p^{n+1} - \boldsymbol{f}_{b}\right) + \frac{\Delta t^{2}}{2}\boldsymbol{u}\cdot\nabla\left(\frac{1}{\rho}\nabla p^{n+1} - \boldsymbol{f}_{b}\right)$$

The increment of the velocity in the n^{th} time step can be spilt into two parts, including the intermediate velocity increment $\Delta \boldsymbol{u}^{*}$ and the correction of the velocity increment $\Delta \boldsymbol{u}^{**}$ which are presented as

1616* MERGEFORMAT ()

$$\Delta \boldsymbol{u}^{*} = \boldsymbol{K}^{n} + \boldsymbol{f}^{n+1}\Delta t$$

1717* MERGEFORMAT ()

$$\Delta \boldsymbol{u}^{**} = \boldsymbol{R}^{n+1}$$

Substituting $\Delta \boldsymbol{u}^{*}$ and $\Delta \boldsymbol{u}^{**}$ to the boundary condition $\boldsymbol{V}^{n+1} = \boldsymbol{U}^{n+1}$,

1818* MERGEFORMAT

$$\boldsymbol{V}^{n+1} = \boldsymbol{U}^{n+1} = \boldsymbol{I}\ \left(\boldsymbol{u}^{n+1}\right) = \boldsymbol{I}\ \left(\boldsymbol{u}^{n} + \boldsymbol{K}^{n} + \boldsymbol{R}^{n+1} + \boldsymbol{f}^{n+1}\Delta t\right)$$

EFOR

MAT ()

The above equation can be rewritten as

1919*

$$I\left(\boldsymbol{f}^{n+1}\Delta t\right)=\boldsymbol{V}^{n+1}-I\left(\boldsymbol{u}^{n}+\boldsymbol{K}^{n}+\boldsymbol{R}^{n+1}\right)$$ MERG

EFOR

MAT ()

Subsequently, the term $I\left(\boldsymbol{f}^{n+1}\Delta t\right)$, which represents the body force on the immersed boundary (IB) points, is distributed to the grid node

2020*

$$D\left(I\left(\boldsymbol{f}^{n+1}\Delta t\right)\right)=D\left(\boldsymbol{V}^{n+1}-I\left(\boldsymbol{u}^{n}+\boldsymbol{K}^{n}+\boldsymbol{R}^{n+1}\right)\right)$$ MERG

EFOR

MAT ()

Then, the formulation of the term $\boldsymbol{f}^{n+1}$ can be written as

2121*

$$\boldsymbol{f}^{n+1}\Delta t=D\left[\boldsymbol{V}^{n+1}-I\left(\boldsymbol{u}^{n}+\boldsymbol{K}^{n}+\boldsymbol{R}^{n+1}\right)\right]$$ MERG

EFOR

MAT ()

It can be observed from Eq. Error: Reference source not found that the extra body force $\boldsymbol{f}$ is coupled with the pressure and an outer loop is needed to solve the variables. The detailed calculation is carried out in the following three steps.

Step 1: predict the intermediate velocity $\boldsymbol{u}^{*,K}$ without considering the pressure and the extra body force.

2222*

MERG

$$\boldsymbol{u}^{*,K}=\boldsymbol{u}^{n}+\boldsymbol{K}^{n}$$ EFOR

MAT

()

Step 2: calculate the pressure increment $\Delta p^{n,k}$ and the extra body force $\boldsymbol{f}^{n+1,k}$ in an iterative way.

Let $p^{n+1,0}=p^{n}$ and $\boldsymbol{f}^{n+1,0}=0$, $k=1$

Outer loop begins

(2-1) calculate the extra body force $\boldsymbol{f}^{n+1,k}$ according to Eq. Error: Reference source not found.

It is not guaranteed that all the immersed boundary points coincide with the grid nodes. Hence, an inner loop should be carried out [40] in this step to meet the boundary condition $\boldsymbol{V}^{n+1}=\boldsymbol{U}^{n+1}$.

Inner loop begins

Let $\boldsymbol{f}^{n+1,k,0}=\boldsymbol{f}^{n+1,k-1}$, $i=1$ and calculate $\boldsymbol{f}^{n+1,k,i}$ according to Eq. Error: Reference source not found

$$\boldsymbol{f}^{n+1,k,i}\Delta t=\boldsymbol{f}^{n+1,k,i-1}\Delta t+D\left[\boldsymbol{V}^{n+1}-I\left(\boldsymbol{u}^{n}+\boldsymbol{K}^{n}+\boldsymbol{R}^{n+1}+\boldsymbol{f}^{n+1,k,i-1}\Delta t\right)\right] \quad (2323\text{*}\ \text{MERGEFORMAT})$$

If $\left\|\boldsymbol{V}^{n+1}-I\left(\boldsymbol{u}^{n}+\boldsymbol{K}^{n}+\boldsymbol{R}^{n+1}+\boldsymbol{f}^{n+1,k,i-1}\Delta t\right)\right\|$ is smaller than a given tolerance ε, where $\|\|$ represents a kind of norms, break the inner loop. Otherwise, let $i=i+1$. Generally, it is enough to repeat the inner cycle 5 to 10 times based on the experiences of the authors.

Inner loop ends

$\boldsymbol{f}^{n+1,k}=\boldsymbol{f}^{n+1,k,i}$

(2-2) update the intermediate velocity $\boldsymbol{u}^{*,n+1,k}$.

$$\boldsymbol{u}^{*,n+1,k} = \boldsymbol{u}^{*,K} + \boldsymbol{f}^{n+1,k}\Delta t$$

242
4*
MERGEFORMAT ()

(2-3) update the intermediate pressure $p^{n+1,k}$ according to the continuity equation.

$$\nabla\cdot\left(\boldsymbol{u}^{*,n+1,k} + \boldsymbol{R}^{n+1,k}\right) = 0$$

252
5*
MERGEFORMAT ()

(2-4) check the convergence.

The convergence is checked on the basis of Eq. Error: Reference source not found. If the condition of convergence is met, break the outer loop. Otherwise, the $k+1^{th}$ iteration of the n^{th} step should be done subsequently.

$$\left\| I\left(\boldsymbol{u}^{n} + \boldsymbol{K}^{n} + \boldsymbol{R}^{n+1,k}\right) - I\left(\boldsymbol{u}^{n} + \boldsymbol{K}^{n} + \boldsymbol{R}^{n+1,k-1}\right)\right\| < \varepsilon$$

2626*
MERGEFORMAT

()

where ε is a given tolerance.

Outer loop ends.

Step 3: update the pressure p^{n+1} and correct the velocity $\boldsymbol{u}^{n+1}$.

2727* MERGEFORMAT ()

$$p^{n+1} = p^n + \Delta p^{n,k}$$

2828* MERGEFORMAT ()

$$\boldsymbol{u}^{n+1} = \boldsymbol{u}^* + \boldsymbol{R}^{n+1,k}$$

2.4 Interaction force between the fluid and the solids

The calculation of the extra force f is illustrated in the previous section, while the formulation of the FSI force is not derived. It should be noted that the interaction forces between the fluid and the solids, including the force acted on the solids by the fluid $\boldsymbol{F}_f$ and the reactive force $\boldsymbol{F}_s$, are different with the extra body force. $\boldsymbol{F}_f$ and $\boldsymbol{F}_s$ are applied on immersed boundary points while f is imposed on the grid node in the Eulerian framework.

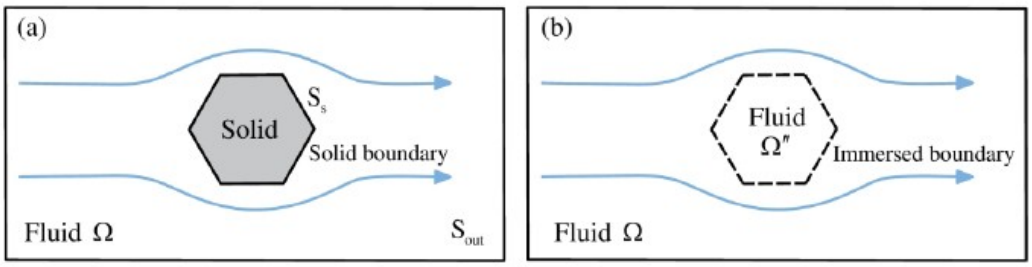

Figure 5 Sketch of the calculation domain. (a) body conformed method; (b) immersed

boundary method. S_s is the solid boundary, S_{out} is the boundary of the calculated domain, Ω is the domain bounded by S_s and S_{out}, Ω'' is the domain inside S_s

In the framework of the BCM shown in Figure 5(a), the force exerted to the fluid by the solids $\boldsymbol{F}_s$ can be written as an integration

2929*

$$\boldsymbol{F}_s = -\int_{S_s} \boldsymbol{n} \cdot \sigma dS$$

MERG

EFOR

MAT ()

where $\boldsymbol{n}$ is the outward normal vector of S_s, $\boldsymbol{\sigma} = -\frac{1}{\rho}\boldsymbol{I}p + \frac{\mu}{\rho}(\nabla \boldsymbol{u} + \nabla^T \boldsymbol{u})$, $\boldsymbol{I}$ is the unit tensor.

In the BCM, the equilibrium of the momentum should be satisfied. The momentum equation, in which the extra body force term is not included, is integrated over the domain

3030*

$$\int_{\Omega}\left(\frac{\partial \boldsymbol{u}}{\partial t} - \boldsymbol{f}_b\right) d\Omega + \int_{S_{out}} \boldsymbol{n} \cdot (\boldsymbol{uu} - \boldsymbol{\sigma})\, dS - \int_{S_s} \boldsymbol{n} \cdot (\boldsymbol{uu} - \boldsymbol{\sigma})\, dS = 0$$

MERG

EFOR

MAT ()

Since S_s is the solid boundary, the condition $\boldsymbol{n} \cdot \boldsymbol{uu} = 0$ should be met. Therefore, the third term of Eq. Error: Reference source not found can be simplified further. Substituting Eq. Error: Reference source not found into Eq. Error: Reference source not found, the term $\boldsymbol{F}_s$ can be written as

3131*

$$\boldsymbol{F}_s = \int_{\Omega}\left(\frac{\partial \boldsymbol{u}}{\partial t} - \boldsymbol{f}_b\right) d\Omega + \int_{S_{out}} \boldsymbol{n} \cdot (\boldsymbol{uu} - \boldsymbol{\sigma})\, dS$$

MERG

EFOR

MAT ()

In the IBM, the whole domain Ω', which is the sum of Ω and the domain Ω'' occupied by the solids in the BCM, is filled with the fluid, shown in Figure 5(b). The equilibrium of the momentum should be satisfied and Eq. Error: Reference source not found is substituted into the integrated result of Eq. Error: Reference source not found

3232*

$$\boldsymbol{F}_s = \int_{\Omega'} \boldsymbol{f} d\Omega - \int_{\Omega''} \left(\frac{\partial \boldsymbol{u}}{\partial t} - \boldsymbol{f}_b \right) d\Omega$$

MERG

EFOR

MAT ()

According to the Newton's third law, the force acted on the solids by the fluid $\boldsymbol{F}_f$ is calculated as

3333*

$$\boldsymbol{F}_f = -\boldsymbol{F}_s = -\int_{\Omega'} \boldsymbol{f} d\Omega + \int_{\Omega''} \left(\frac{\partial \boldsymbol{u}}{\partial t} - \boldsymbol{f}_b \right) d\Omega$$

MERG

EFOR

MAT ()

where the terms $\int_{\Omega''} \frac{\partial \boldsymbol{u}}{\partial t} d\Omega$ and $\int_{\Omega''} \boldsymbol{f}_b d\Omega$ forces are exerted on the fluid inside the immersed boundary, which represent the inertia force and the effect of the buoyancy, respectively.

2.5 Iterative scheme for the coupling system

To solve the coupled fluid-solid system and realize the strong coupling between the fluid and the solids, an iterative scheme should be carried out. The governing equations of the fluid are discretized spatially based on the standard Galerkin procedure

3434*

$$(\Delta \boldsymbol{u}, \Delta p) = \boldsymbol{RHS}_f (\boldsymbol{u}, p, \boldsymbol{\delta})$$

MERG

EFOR

MAT ()

According to the velocity Verlet algorithm [44], the governing equation of the solids is discretized as

3535*

$$\Delta \boldsymbol{\delta} = \boldsymbol{RHS}(\boldsymbol{\delta}, \boldsymbol{F}_f) = \boldsymbol{RHS}_s (\boldsymbol{\delta}, \boldsymbol{u}, p)$$

MERG

EFOR

MAT ()

Hence, the iterative scheme for the coupling system is

3636*

$$(\Delta \boldsymbol{u}^{n,k}, \Delta p^{n,k}) = \boldsymbol{RHS}_f\left(\boldsymbol{u}^n, p^n, \boldsymbol{\delta}^{n+1,k-1}\right)$$ MERG EFOR MAT ()

3737*

$$\Delta \boldsymbol{\delta}^{n,k} = \boldsymbol{RHS}_s\left(\boldsymbol{\delta}^n, \boldsymbol{u}^{n+1,k}, p^{n+1,k}\right)$$ MERG EFOR MAT ()

Supposing the calculation of the n^{th} step has been finished, the k^{th} iteration of the $n+1^{th}$ step is carried out.

Loop begins

Step 1: solve the equation of the fluid phase (Eq. Error: Reference source not found).

Let $\boldsymbol{\delta}^{n+1,0} = \boldsymbol{\delta}^n$.

The right-hand scheme of Eq. Error: Reference source not found is calculated and the influence of the solid motion on the fluid phase is considered. Both the velocity and the pressure of the fluid field are updated as follows

3838*

$$\boldsymbol{u}^{n+1,k} = \boldsymbol{u}^n + \Delta \boldsymbol{u}^{n,k}$$ MERG EFOR MAT ()

3939*

$$p^{n+1,k} = p^n + \Delta p^{n,k}$$ MERG EFOR MAT ()

Step 2: solve the equation of the solids (Eq. Error: Reference source not found).

The right-hand scheme of Eq. Error: Reference source not found is calculated

which reflects the influence of the fluid field, including the velocity and the pressure, on the solids. Then, the motion of the solids is updated according to Eq. Error: Reference source not found

$$\boldsymbol{\delta}^{n+1,k} = \boldsymbol{\delta}^{n} + \Delta\boldsymbol{\delta}^{n,k} \quad (4040\text{*MERGEFORMAT})$$

Step 3: check the convergence.

The convergence is checked on the basis of Eq. Error: Reference source not found. If the condition of convergence is met, break the loop.

$$\left\| \Delta\varsigma^{n,k} - \Delta\varsigma^{n,k-1} \right\| < \varepsilon_{\varsigma} \quad (4141\text{*MERGEFORMAT})$$

where ς is $\boldsymbol{u}$, p or $\boldsymbol{\delta}$, ε_{ς} is a small value for the corresponding variable ς.

Step 4: carry out the $k+1^{th}$ iteration of the $n+1^{th}$ step.

Let $k = k+1$ and repeat Step 1 to Step 3.

Loop ends

It should be noticed that the velocity $\boldsymbol{u}^{n+1,k}$ and the pressure $p^{n+1,k}$ only depend on $\boldsymbol{u}^{n}$, p^{n} and $\boldsymbol{\delta}^{n+1,k-1}$, instead of $\boldsymbol{u}^{n+1,k-1}$ and $p^{n+1,k-1}$. On the contrary, the movement of the solids $\boldsymbol{\delta}^{n+1,k}$ depends on $\boldsymbol{\delta}^{n}$, $\boldsymbol{u}^{n+1,k}$ and $p^{n+1,k}$, instead of $\boldsymbol{\delta}^{n+1,k-1}$.

3 Numerical cases

3.1 Flow past a static cylinder

As a benchmark case, the laminar flow past a static cylinder has been studied widely in decades and it is simulated herein to demonstrate the validity of the IBM and the ability of the proposed method in modelling the interaction between the fluid and the fixed solid.

The flow is characterized according to the Reynolds number $\mathrm{Re}=\frac{\rho U_\infty D}{\mu}$, where ρ and μ are the density and the dynamic viscosity of the fluid, U_∞ is the far-field velocity and D is the diameter of the cylinder. The size of the calculated domain is $60D\times 40D$ and the centroid of the cylinder is located $15D$ away from the inlet boundary and $20D$ away from the upper and the lower boundaries. According to the suggestions of Persillon and Braza [45], the influence of boundary conditions can be ignored when the width of the computational domain is not smaller than $22D$ and the distance between the centroid of the cylinder and the outflow boundary is larger than $34D$ in the condition of $\mathrm{Re}=100$. Obviously, the above two conditions are met in the current simulation, which means the calculated domain can be regarded as infinite and the sensitivity of the results to the domain size can be eliminated.

The domain around the cylinder is discretized by fine rectangles with a size of *D*/ 80 and the mesh is stretched in all four directions towards the boundaries. The whole domain is discretized into 816×448 structural quadrilateral elements. Moreover, 753 immersed boundary points are allocated on the boundary of the cylinder and no less than one immersed boundary point should be located in each element. The inlet boundary is set as a Dirichlet boundary. The top and the bottom boundaries are in the free-slip condition, along with a free outflow boundary.

The general parameters applied to prove the accuracy of the current test case include the drag coefficient C_D, the lift coefficient C_L and the Strouhal number St. The formulations for the above three coefficients are

4242* MERGEFORMAT ()

$$C_D = \frac{2F_D}{\rho U_\infty^2 D}, \quad C_L = \frac{2F_L}{\rho U_\infty^2 D}, \quad St = \frac{f_{req} D}{U_\infty}$$

where f_{req} is the vortex shedding frequency, F_D and F_L are the drag force and the lift force.

The drag coefficient, lift coefficient and the Strouhal number for three different Reynolds number calculated by the current method are listed in Table 1 and the results are compared with those provided in previous references. Since the boundary condition applied in the BCM is more accurate than those in the IBM, the results given by the BCM can be treated as references when the results of the physical experiment are insufficient. It can be observed from Table 1 that the drag coefficient C_D calculated by the IBM is slightly larger than that provided by the BCM. In the IBM, the extra body force is posed on the grid nodes in a band with a certain width around the fluid-solid boundary. Hence, the fluid-solid interface is immersed in the band which enlarges the diameter of the cylinder and leads to the exaggeration of the drag coefficient C_D. However, the lift coefficient and the Strouhal number are hardly affected by the diameter of the cylinder. As a result, the current results of these two parameters are similar with those in different references. Meanwhile, the vortex shedding frequency as expressed into the Strouhal number also agrees very well.

Method	Re =100			Re =150			Re =200		
	C_D	C_L	St	C_D	C_L	St	C_D	C_L	St
BCM [46]	1.350±0.012	0.339	0.165	1.33±0.03	0.53	0.182	1.31±0.049	0.69	0.192
Experiment [47]	-	-	0.166	-	-	0.183	-	-	0.197
IBM [40]	1.402±0.010	0.349	0.167	1.385±0.027	0.538	0.186	1.391±0.047	0.699	0.198
IBM [48]	1.453±0.011	0.339	0.169	-	-	-	-	-	-
IBM (current results)	1.399±0.010	0.339	0.168	1.404±0.028	0.527	0.184	1.438±0.048	0.684	0.196

Table 1. Drag coefficient, lift coefficient and Strouhal number provided by different methods

The instantaneous streamlines and the velocity vectors at $t = 350$ in the

condition of $\mathrm{Re}=100$ are plotted in Figure 6(a) and Figure 6(b), respectively. It can be observed that the streamlines near the fluid-solid interface are conformed to the boundary of the cylinder and no streamline penetrates the interface, which coincides with the practical situation. Meanwhile, the velocity on the immersed boundary is zero, showing that the boundary condition is satisfied on the fluid-solid interface.

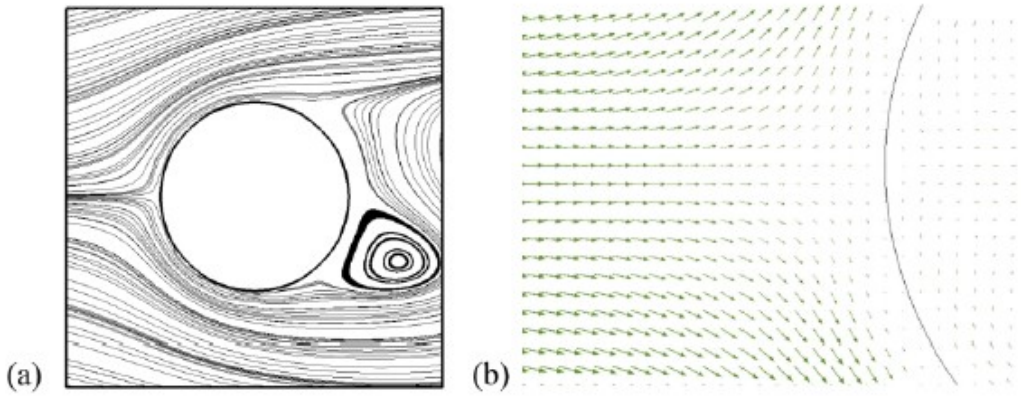

Figure 6 Streamlines and velocity vectors at $t=350$ ($\mathrm{Re}=100$). (a) sketch of streamlines; (b) sketch of velocity vectors

In Figure 6(a), an external vortex can be observed, which is part of the Karman vortex street. In Figure 7, the stable Karman vortex street at $t=350$ for $\mathrm{Re}=100$ is seen, showing a clear vortex shedding phenomenon in the wake of the cylinder as expected.

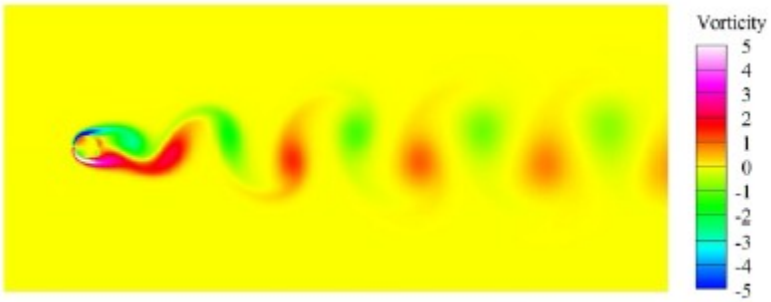

Figure 7 Stable Karman vortex street at $t=350$ ($\mathrm{Re}=100$)

3.2 Vortex-induced vibration of a cylinder

The accuracy of the interaction force calculation between the fluid and the fixed

cylinder has been demonstrated in Section 3.1. However, the cylinder is static, which means the movement of the solid and the interaction between the fluid and the moving solid are not reflected. To demonstrate the ability of the RCFDEM method in solving the solid movement and the FSI effect, the vortex-induced vibration (VIV) of an elastically mounted cylinder is calculated. The cylinder is treated as a mass-spring-damper system and it can move in the horizontal and vertical directions, marked as the *x* direction and the *y* direction respectively. The movement is governed by the equations below

4343* MERGEFORMAT ()

$$\frac{d^2X}{dt^2}+2\xi\left(\frac{2\pi}{U^*}\right)\frac{dX}{dt}+\left(\frac{2\pi}{U^*}\right)^2 X=\frac{2}{\pi m^*}C_D$$

4444* MERGEFORMAT ()

$$\frac{d^2Y}{dt^2}+2\xi\left(\frac{2\pi}{U^*}\right)\frac{dY}{dt}+\left(\frac{2\pi}{U^*}\right)^2 Y=\frac{2}{\pi m^*}C_L$$

in which $\xi=\frac{c}{2\sqrt{km_s}}$ is the damping ratio, *c* is the damping coefficient, $U^*=\frac{U_\infty}{f_N D}$ is the reduced velocity, $f_N=\frac{1}{2\pi}\sqrt{\frac{k}{m_s}}$ is the natural vibration frequency of the cylinder, *k* is the spring stiffness coefficient, *D* is the diameter of the cylinder, $X=x/D$ and $Y=y/D$ are the non-dimensional displacements of the cylinder center, *x* and *y* are the displacements in the corresponding directions, $m^*=m_s/m_f$ is the mass ratio.

In this test case, the calculation domain and the boundary conditions in Section 3.1 are adopted. The remaining parameters are adopted from reference [49]. The

Reynolds number is 200, the damping ratio ξ is 0.01, the reduced velocity U^* is 5.0 and the mass ratio m^* is $4/\pi$. According to the governing equations, the following parameters can be derived. The ratio of the damping coefficient to the solid mass c/m_s is $\pi/125$ and the spring constant *k* is $4\pi^2/25$. Three different mesh resolutions, L1, L2 and L3 are applied to analyze the mesh size sensitivity. The corresponding numbers of quadrangular elements are 204×112, 408×224 and 816×448, and the element size surrounding the cylinder is *D*/20, *D*/40 and *D*/80, respectively.

Initially, the cylinder is fixed and the simulation in Section 3.1 is carried out until a stable Karman vortex street is formed. Afterwards, the cylinder is released and vibrates translationally in the streamwise and transverse directions. The instantaneous vorticity field in shown in and the classic vortex shedding phenomenon, namely the 2S pattern, can be observed near the maximum upper position of the cylinder. The vibration frequency of the cylinder is 0.187, which matches the vortex shedding frequency exactly. Hence, the current simulation is in the synchronization regime of vortex-induced vibration.

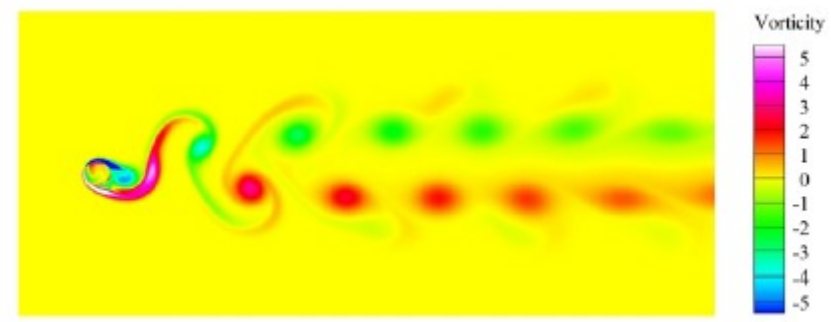

Figure 8 Vorticity field with L3 for a free oscillating cylinder

Considering the existence of the drag force, the vibration center of the cylinder is drifted away from (0,0). In the calculation, the spring extension caused by the initial drag force is deducted and the value is 0.455*D*. The center displacement of the

cylinder in the condition of L3 is given in . It can be observed that the cylinder vibrates stably around (0.177*D*, 0). Hence, the actual oscillation center is (0.632*D*, 0) and it is similar with (0.62*D*, 0) in reference [50], where a spectral element method was applied. In Figure 10, the stable trajectories of the cylinder center in the case of L1, L2 and L3 are plotted and the present results are compared with the existing ones [49,50]. All the centers of the figure-eight-type oscillation are shifted to (0,0) for the convenience of comparison. Blackburn and Karniadakis [50] solved the VIV problem with the spectral element method while an immersed boundary method is employed by Yang et al. [49] and also in our proposed method. Since the mesh size of L1 is relatively coarse, the vortexes are not captured precisely, which leads to the reduction of the displacement in both directions. The current results agree with the previous ones satisfactorily for meshes of L2 and L3, which indicates that the mesh refinement can improve the accuracy significantly. Meanwhile, the accuracy of our proposed method in dealing with the FSI problems with moving objects has been further verified.

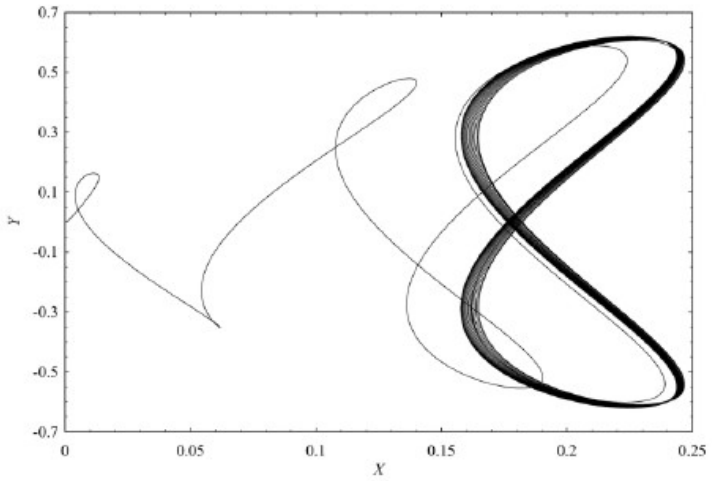

Figure 9 Centerline displacement phase plot

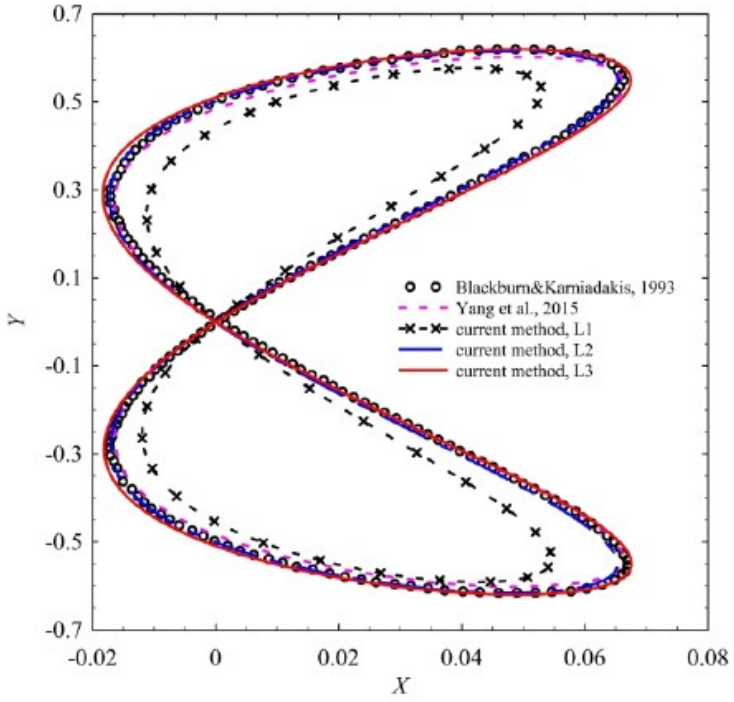

Figure 10 Centerline displacement phase plot after the transient

3.3 Sedimentation of a circular particle

In the previous VIV test case, the cylinder is bounded by two springs and it vibrates in a confined area. To assess the ability of the proposed RCFDEM method in dealing with the interaction between the fluid and the solid with large movement, the sedimentation of a circular particle is simulated.

The parameters are same with those given by Glowinski etc. [51]. The calculation domain is 0.02 m×0.06 m. The coordinate of the bottom left corner is (-0.01 m, 0). The diameter of the circular particle is 0.0025m. Initially, the center of the particle is located at (0, 0.04m) and the flow velocity of the whole flow field is 0. The density of the fluid is 1000kg/m^3, the dynamic viscosity is $0.01\mathrm{kg}/(\mathrm{m}\cdot\mathrm{s})$ and the density of the rigid particle is 1250kg/m^3. The particle is released from rest and is driven by the gravity to fall. The calculated domain is discretized into 384×1152 structured quadrilateral elements and 452 immersed boundary points are placed on the boundary of the particle. The element size surrounding the particle is *D*/48. All the

boundaries of the channel are modeled as non-slip solid walls.

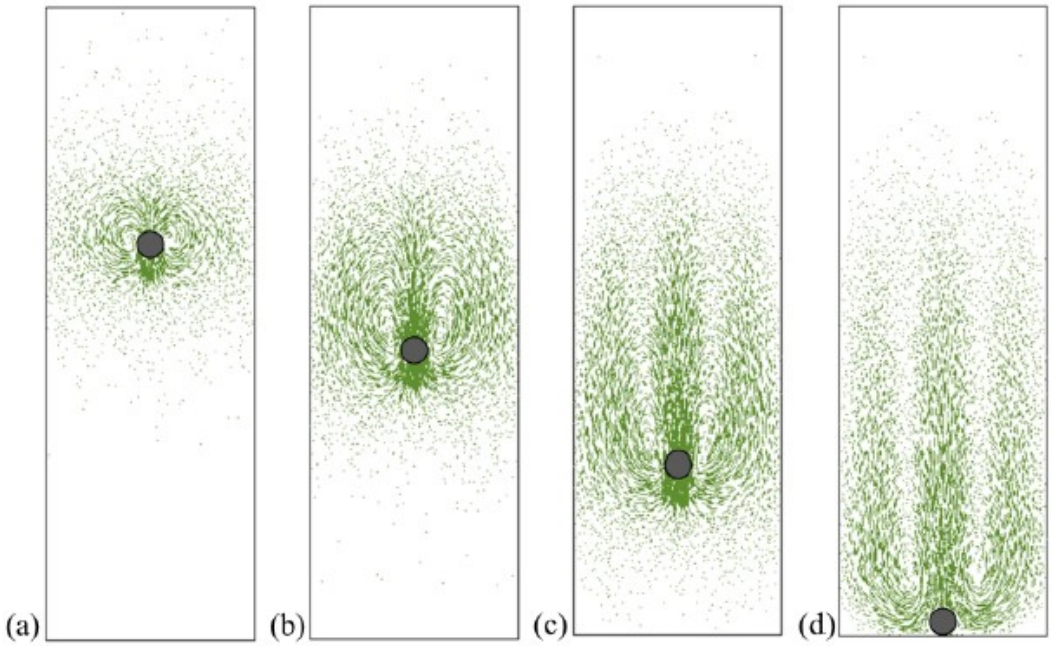

Figure 11 Field of the velocity vector at different time

The velocity vector field and the position of the particle at four different time are shown in . The particle is released from static state at $t=0$, then moves freely under the effect of the gravity. As time progresses, the velocity of the particle keeps increasing and two vortexes can be observed on the left and right side of the particle. The sedimentation of the particle disturbs the flow field more obviously as time passes by. At $t=0.8$ s, the particle has already hit the bottom of the domain.

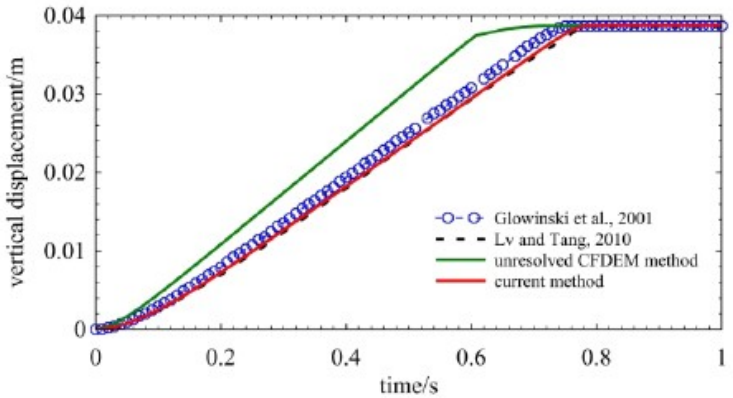

Figure 12 Vertical displacement of the particle versus time

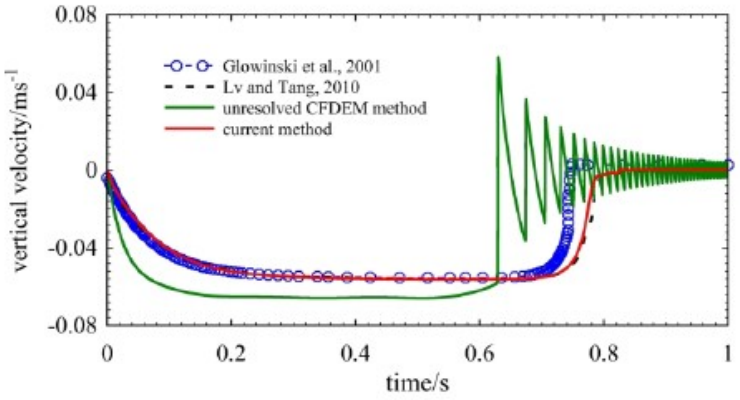

Figure 13 Vertical velocity of the particle versus time

The current calculated results are compared with those given by Glowinski etc. [51] and Lv and Tang [52]. The vertical displacement and the vertical velocity of the particle versus time are given in Figure 12 and Figure 13 respectively. It can be seen from Figure 12 and Figure 13 that the results calculated by our proposed RCFDEM method agree well with those in the reference [51] and the reference [52]. Figure 13 shows that the particle reaches a uniform velocity quickly after it is released. Then, the particle keeps this velocity until it is deposited at the bottom at $t = 0.73$ s. After 0.73 s, the vertical velocity of the particle changes to 0 in a short period. The results calculated by the unresolved CFDEM model is also included in Figure 12 and Figure 13. It can be observed from Figure 12 that the general tendencies of the particle movement calculated by different methods are similar. The vertical velocity calculated by the RCFDEM method decreases gradually as the particle approaches the bottom. The gradual decreasing velocity is induced by the ground effect which means a significant lift force is exerted to the particle. On the contrary, the vertical velocity given by the unresolved CFDEM method plummets when the particle arrives the bottom. The divergence of the velocity evolution is caused by the different calculation methods of the particle-fluid interaction force. In the unresolved CFDEM method, the force calculation is based on the velocity difference between the particle and the averaged fluid field which is approximate to zero when the particle is sedimented to

the bottom. As a result, the interaction force, which can decrease the vertical velocity of the particle, does not exist in the unresolved CFDEM method. Subsequently, the oscillation of the vertical velocity provided by the unresolved CFDEM method can be seen in Figure 13 which is attributed to the viscous dissipation of the fluid field.

Even though the results calculated by the proposed RCFDEM method coincide with the previous numerical outcomes better than the results of the unresolved method, the overall performance of the unresolved method in modelling the interaction between the fluid and a single particle is still acceptable in terms of displacement.

3.4 Drafting-kissing-tumbling of two particles

Only one particle was included in the previous test case and the complex interaction between solids were not dealt. Therefore, a benchmark test concerning the sedimentation of two particles is calculated and the classic drafting-kissing-tumbling phenomenon is studied in this subsection. The difference between the unresolved CFDEM method and the RCFDEM method is further illustrated.

The calculation domain is 0.02 m×0.08 m and coordinate of the bottom left corner is defined as (0, 0). Originally, the center coordinates of the lower particle P1 and the upper particle P2 are (0.01 m, 0.068 m) and (0.01 m, 0.072 m), respectively. The diameter of the two circular particles is 0.002 m and the density is $1010\ \mathrm{kg/m^3}$. The density of the fluid is $1000\ \mathrm{kg/m^3}$ and the dynamic viscosity is $0.001\mathrm{kg/(m\cdot s)}$. The normal and shear stiffness of the particles are set as 2×10^7 Pa. The internal friction angle and the damping ratio are 0. The particles are released from rest and are driven by the gravity force. The calculated domain is discretized into 256×1024 structured quadrilateral elements and 241 immersed boundary points are spread on the boundary of each particle. The element size surrounding the particles is *D*/25.6. The boundaries in the longitudinal direction are modeled as non-slip solid walls, while the

boundaries in the transverse direction are periodic.

The velocity vector of the whole domain calculated by the RCFDEM method is shown in . The vorticities around the particles are described clearly which demonstrate that the proposed method is capable of simulating the flow surrounding particles precisely.

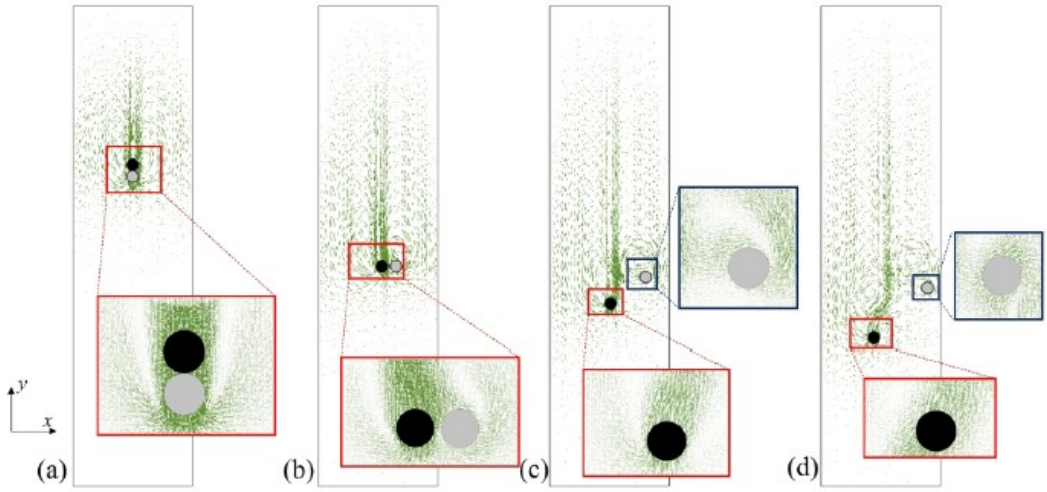

Figure 14 Field of the velocity vector at different time

Meanwhile, the classic drafting-kissing-tumbling (DKT) phenomenon can be observed during the sedimentation process in . To describe the DKT phenomenon quantitatively, the evolution of the relative position between P1 and P2 are drawn in , including the transverse and longitudinal distances between the particles, namely D_x and D_y, and the straight-line distance D_r which can be calculated according to D_x and D_y.

Initially, P1 and P2 move individually under the effect of the gravity. The movement of these two particles leads to a change in the surrounding flow and a low-pressure wake is formed between P1 and P2. Hence, the trailing particle P2 falls faster than the leading particle P1 and this process is named as the drafting process. Subsequently, P2 catches up with P1 at $t = 1.2$ s and this moment is known as kissing. The two particles keep a long body and sediment together till $t = 2.4$ s which is called tumbling. During this stage, the distance between P1 and P2 equals to zero. Finally,

P1 and P2 separate as the stage of tumbling becomes unstable.

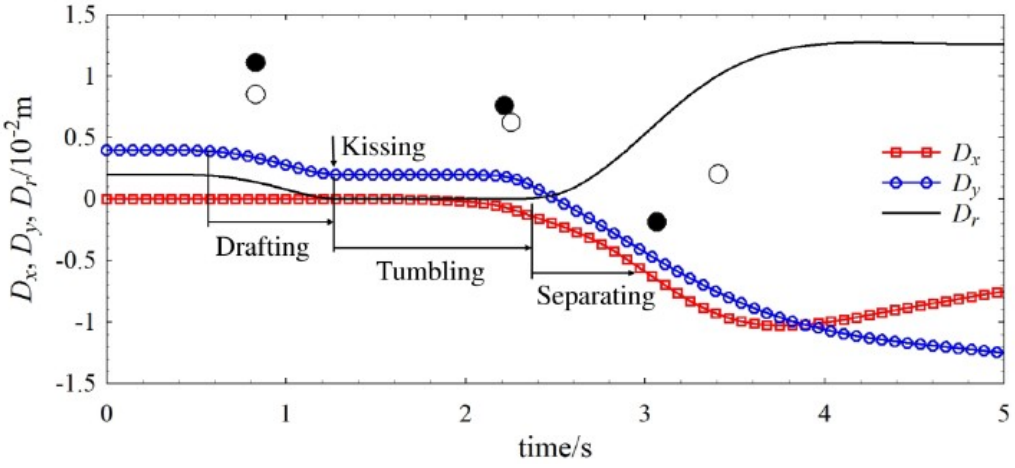

Figure 15 Distance between the particles versus time

To further prove the accuracy of the RCFDEM method, the coordinates of the two particles versus time are plotted in and the present results are compared with those provided by Jafari et al. [53] and Wang et al. [54]. A great agreement is achieved in both the transverse and the longitudinal coordinates with only small differences. The transverse coordinates of the leading particle P1 suffers slight divergence during the separating process. This phenomenon is attributed to the different numerical methods in simulating the fluid phase and the fluid-particle interaction. In references [53] and [54], the lattice Boltzmann method is coupled with different collision models to simulate the sedimentation of the particles, while the behavior is predicted by the new RCFDEM method. Meanwhile, the results calculated by the unresolved CFDEM method are also included in and the weakness of the unresolved CFDEM method is revealed. Using the unresolved CFDEM method, P1 and P2 are sedimented without the DKT process. This inaccuracy is induced to the limitation of the empirical formulation used to calculate the interaction force. The formulation is proposed for only one circular particle, whereas the contact between the two particles and the complexity of the fluid flow triggered by the solids cannot be reflected in the unsolved method.

This test case illustrates that the unresolved CFDEM method is unable to model

the complex fluid field affected by particles, while the newly proposed RCFDEM method is robust in simulating the evolution of the fluid, the motion of particles and the interaction between the fluid and the moving particles.

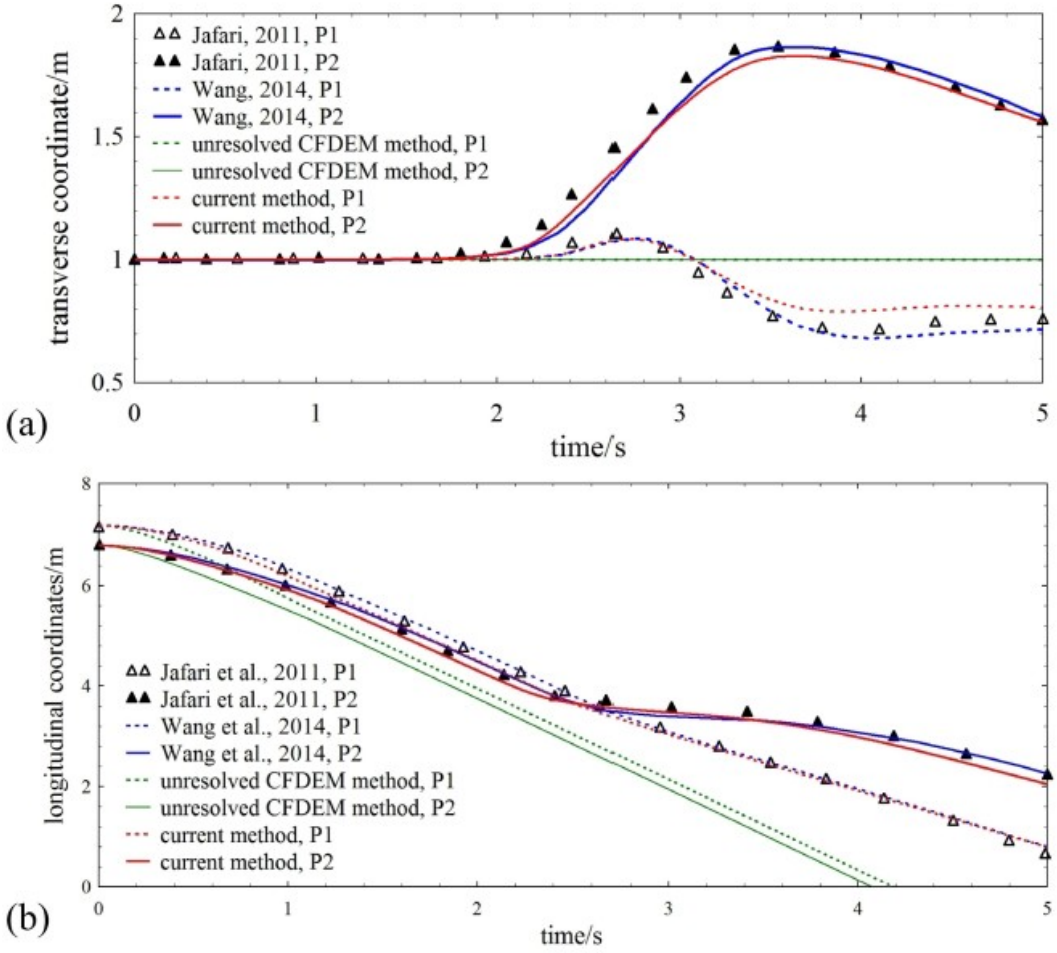

Figure 16 Coordinates of the particles versus time. (a) transverse coordinates; (b) longitudinal coordinates

3.5 Sedimentation of multiple solids

In this section, the number of the solids increases to 64 and the sedimentation process is simulated. Initially, the ability of the RCFDEM method in coping with the interaction between the fluid and a large number of rigid bodies is illustrated. All the rigid bodies are chosen as circular particles and the packing process is compared between the unresolved method and the RCFDEM approach. Thereafter, the

sedimentation of 64 square solids is calculated to demonstrate the feasibility of the proposed method in modeling the interaction between the fluid and the solids with arbitrary shapes.

3.5.1 Sedimentation of circular rigid particles

The sedimentation of the 64 rigid particles with different diameters are calculated by the unresolved CFDEM method and the proposed RCFDEM method separately. The initial set up of this case is shown in . The 64 particles are placed in an enclosed 10m×10m box and they can be divided into two groups according to the diameter, 0.550 m and 0.275 m. The fluid density is 1000kg/m^3 and the density ratio of particle to fluid is 2.6. The dynamic viscosity of the fluid is $0.01\mathrm{kg}/(\mathrm{m}\cdot\mathrm{s})$. The normal and shear stiffness of the particles are set as 4.8×10^8 Pa. All the boundaries are treated as non-slip solid walls. Both the fluid and the particles are stationary at $t=0$ and the 64 rigid particles are driven by the gravity.

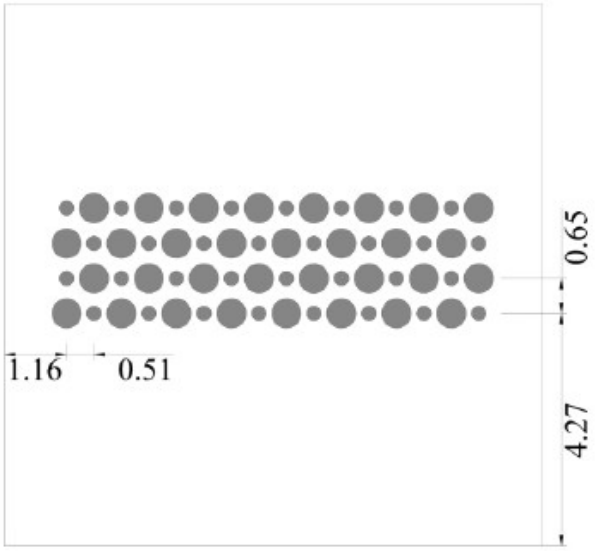

Figure 17 Initial position of 64 rigid circular particles in an enclosure. The unit is m

In the unresolved method, the calculation domain is discretized into 144×144 structural square elements. The simulation results are depicted in several snapshots,

shown in . It can be found from the close-up examination of (a) that almost all of the velocity vectors are vertical, demonstrating that the size of particles does not have an influence on the velocity field. Actually, the particles are simplified to the corresponding centers and the actual size is not reflected in the simulation. In other words, the fluid flow cannot feel the existence of the solid bodies. The final deposit status is shown in (e).

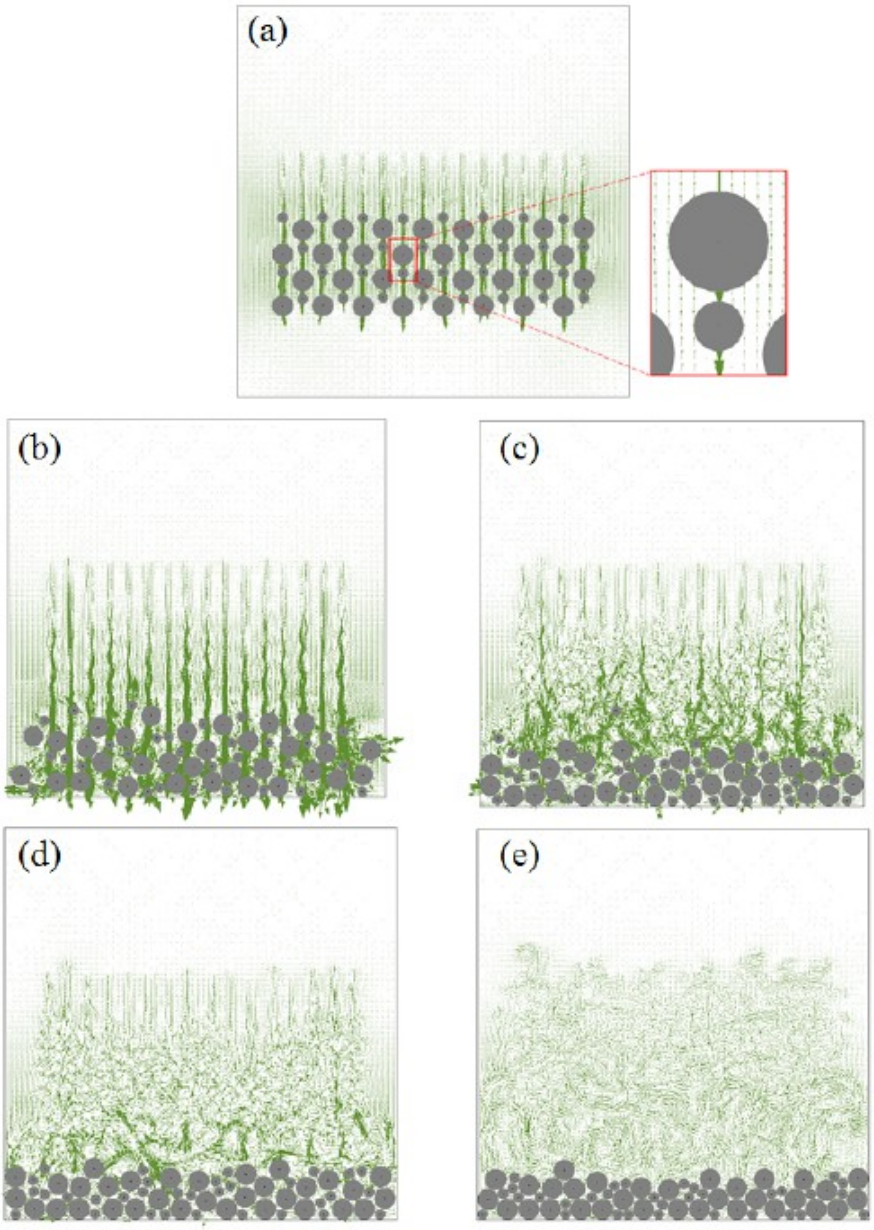

Figure 18 Position of circular particles calculated by the unresolved CFDEM method.

(a) $t = 1.00$ s; (b) $t = 2.02$ s; (c) $t = 3.02$ s; (d) $t = 4.02$ s; (e) $t = 10.00$ s

The same simulation is then carried out by employing the proposed RCFDEM method. The calculation domain is discretized into 480×480 structural square elements and 584 and 1551 immersed boundary points are allocated on the surface of each small and large particle respectively.

The instantaneous field of velocity vectors are given in . The velocity vectors around the particles are not as vertical as those provided by the unresolved method, even in the initial stage shown in (a). Hence, the actual size is considered in the current method. As particles settle due to the gravity force, the velocity field becomes complicated and the particles are distributed in the enclosure irregularly ((b)). The velocity vectors among the particles are enlarged in (c) and a vortex can be observed clearly. Initially, the eddies are created due to the movement of particles. Subsequently, the vortexes develop and drive the particles. At $t = 3.02$ s ((d)), a particle can be found in the top right corner of the enclosure and it continues to move upwards as time goes on ((e)). This phenomenon is caused by the vortex surrounding this particle, which is able to shoot the particle upwards. Since the particle diameter influences the settling velocity, an obvious particle screening phenomenon can be seen during the sedimentation process. Most of the 64 particles sink to the bottom at $t = 5.04$ s and the final status at $t = 15.04$ s is shown in (f). Due to the precise simulation of the complex fluid field and the FSI effect, the duration of the sedimentation calculated by the RCFDEM method is longer than that of the unresolved method.

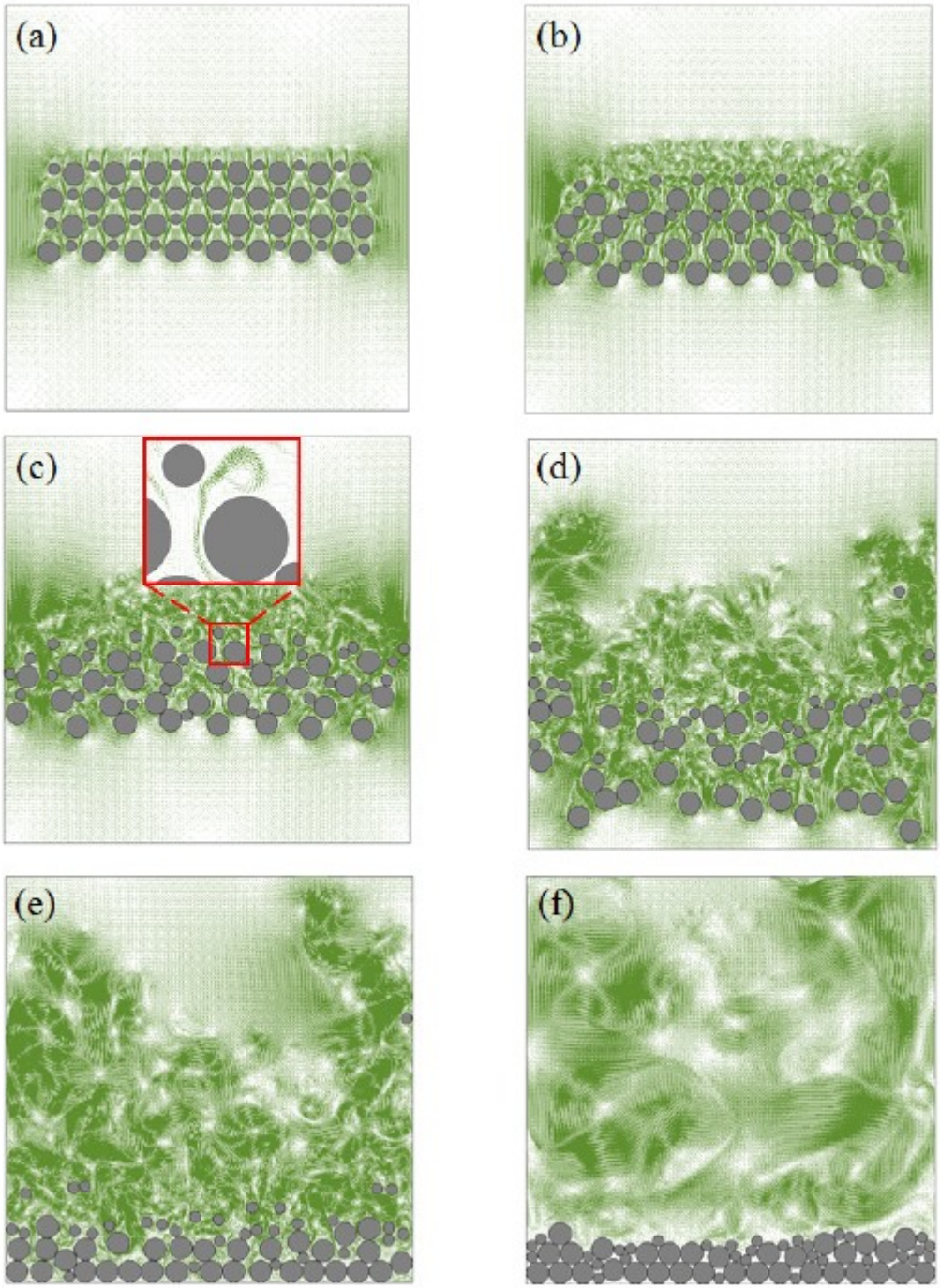

Figure 19 Position of circular particles calculated by the proposed RCFDEM method.

(a) $t = 0.50$ s; (b) $t = 1.01$ s; (c) $t = 1.51$ s; (d) $t = 3.02$ s; (e) $t = 5.04$ s; (f) $t = 15.04$ s

Compared with the unresolved method, the fluid field is resolved and the fluid phase surrounding the particles is simulated precisely in the RCFDEM method.

Moreover, the influence of the wake flow on particles can be considered. Hence, the proposed method displays a strong accuracy advantage in simulating the interaction between the fluid and the dense particles.

3.5.2 Sedimentation of square rigid bodies

The unresolved CFDEM method is limited to circular particles because of the dependence of the interaction force calculation on empirical formulas. In this part, the sedimentation of the 64 rigid square solids with different size is simulated with the proposed RCFDEM method. The initial distribution of the 64 rigid square bodies is given in . The length of the large squares and the small squares is 0.550 m and 0.275 m, respectively. The calculation domain, the boundary condition and the material properties of the fluid and the rigid bodies are the same with those in Section 3.5.1. The whole domain is discretized into 480×480 structural square elements and 810 and 1376 immersed boundary points are allocated on the surface of each small and large square respectively.

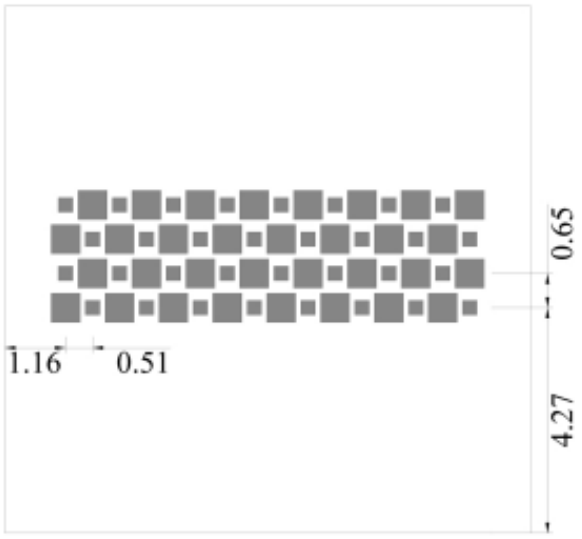

Figure 20 Initial position of 64 rigid square bodies in an enclosure. The unit is m

The velocity vectors at different times are listed in and the body motion is similar with that of the circular particle calculated by the proposed method. The velocity vectors sidestep the rigid bodies during the sedimentation process ((a)-(f)), instead of passing through the solid bodies as in . The velocity vectors near the left

and right walls are upward and the sedimentation of the solid bodies near the walls is hindered, as shown in (b)-(c). The body movement lead to the complexification of the fluid field in the enclosure and a large number of vortexes can be observed ((c)-(d)). Then, the movement of solid bodies is influenced by the created vortexes. Most of the squares reach the bottom at $t = 8.85$ s as shown in (e). Afterwards, the disorder of the fluid field decreases gradually since part of the squares stay static. The final status of the sedimentation is given in (f).

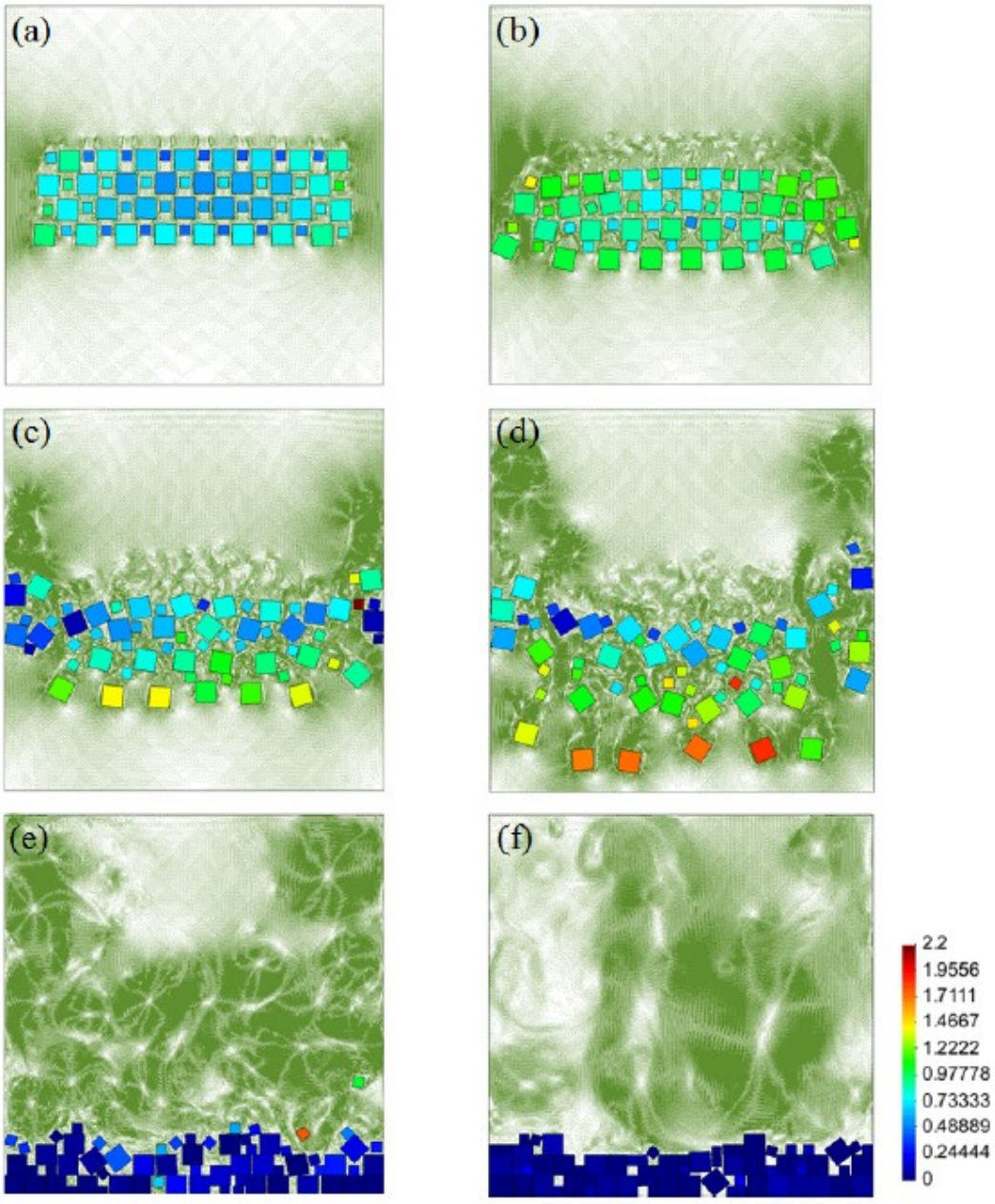

Figure 21 Instantaneous velocity vectors and the velocities of the rigid bodies. The color of the rigid bodies indicates the value of the velocity from dark red for 2.2 m/s to dark blue for 0 m/s. (a) $t = 0.50$ s; (b) $t = 1.21$ s; (c) $t = 2.02$ s; (d) $t = 3.02$ s; (e) $t = 8.85$ s; (f) $t = 21.49$ s

In this simulation, the interaction between the fluid and the square bodies are represented properly. It was shown that the proposed RCFDEM method can be used to model the complicated fluid field and the moving solid boundaries with arbitrary shapes.

4 Conclusions

The main difficulties in handling the fluid-solid interaction problems lie in the description of the solid boundaries with large movement and the reflection of the strong coupling of the system for the fluid and the discontinuous solids. In this paper, a resolved model named as the RCFDEM approach is proposed, which is a combination of the computational fluid dynamics and the discrete element method. The above key challenges are properly solved using the immersed boundary method (IBM) and the iterative partitioned method. Considering the different mechanical properties, the Navier-Stokes equations were employed to model the fluid flow which was discretized in the Eulerian framework, while the discrete element method using the Lagrangian description was utilized to simulate the solids. To describe the moving fluid-solid interfaces and to couple the methods in different frameworks, the IBM was applied. With the application of the IBM, the boundary conditions on the immersed boundary points should be satisfied and the fluid-solid interaction force can be calculated on this basis. To achieve a strong coupling of the fluid and the solids, the coupled system was solved by the partitioned method in an iterative way. The accuracy of the proposed method in managing the fluid-solid interaction problems

was verified by four classic test cases, namely, flow past a static cylinder, the vortex-induced vibration of a cylinder, the sedimentation of a circular particle and the drafting-kissing-tumbling phenomenon of two particles. Finally, the RCFDEM method was employed to simulate the sedimentation of multiple rigid bodies. Compared with the previous unresolved CFDEM methods which depend on empirical equations, the flow field surrounding the solids is captured with high resolution and the true bilateral fluid-solid interaction can be precisely considered in the newly proposed resolved method. Moreover, the current method can describe the solid boundaries with large movement and arbitrary shapes. To ensure the high resolution of the RCFDEM method and the strong coupling phenomenon between the fluid and the solids, the fluid mesh around the solids should be fine and several iterations should be accomplished. Even though the computational cost increases for the sake of accuracy, the parallel technique will be developed for the RCFDEM method in the future to reduce the computational consumption.

5 Acknowledgement

This work was supported by the National Key R&D Program of China (Grant No. 2018YFC0406705); China Postdoctoral Science Foundation Funded Project (Grant No. 2019M651677); Fok Ying-Tong Education Foundation for Young Teachers in the Higher Education Institutions of China (Grant No. 151073); and the Priority Academic Program Development of Jiangsu Higher Education Institutions (Grant No. YS11001) and Qing Lan Project.

6 References

1. Wang DY, Wu CQ, Huang WC, Zhang YS. Vibration investigation on fluid-structure interaction of ap1000 shield building subjected to multi earthquake excitations. Ann Nucl Energy 2019;126: 312-329.

2. Yang P, Xiang J, Fang F, Pain CC. A fidelity fluid-structure interaction model for vertical axis tidal turbines in turbulence flows. Appl Energy 2019;236: 465-477.
3. Taelman L, Degroote J, Swillens A, Vierendeels J, Segers P. Fluid-structure interaction simulation of pulse propagation in arteries: Numerical pitfalls and hemodynamic impact of a local stiffening. Int J Eng Sci 2014;77: 1-13.
4. Bazilevs Y, Takizawa K, Tezduyar TE. Challenges and directions in computational fluid-structure interaction. Math Models Methods Appl Sci 2013;23(2): 7.
5. Li S, Karney BW, Liu G. Fsi research in pipeline systems - a review of the literature. J Fluids Struct 2015;57: 277-297.
6. Ilie M. Fluid-structure interaction in turbulent flows; a cfd based aeroelastic algorithm using les. Appl Math Comput 2019;342: 309-321.
7. Lee K, Huque Z, Kommalapati R, Han SE. Fluid-structure interaction analysis of nrel phase vi wind turbine: Aerodynamic force evaluation and structural analysis using fsi analysis. Renew Energ 2017;113: 512-531.
8. Tao S, Zhang HL, Guo ZL, Wang LP. A combined immersed boundary and discrete unified gas kinetic scheme for particle-fluid flows. J Comput Phys 2018;375: 498-518.
9. Dash SM. A flexible forcing immersed boundary-simplified lattice boltzmann method for two and three-dimensional fluid-solid interaction problems. Comput Fluids 2019;184: 165-177.
10. Mohaghegh F, Udaykumar HS. Modeling collisions of arbitrary-shaped particles in simulations of particulate flows. Powder Technol 2019;344: 756-772.
11. Stabel J, Ren M. Fluid-structure-interaction for the analysis of the dynamics of fuel storage racks in the case of seismic loads. Nucl Eng Des 2001;206(2): 167-176.
12. Basting S, Quaini A, Canic S, Glowinski R. Extended ale method for fluid-structure interaction problems with large structural displacements. J Comput Phys 2017;331: 312-336.
13. Bazilevs Y, Korobenko A, Deng X, Yan J. Novel structural modeling and mesh moving techniques for advanced fluid-structure interaction simulation of wind

turbines. Int J Numer Methods Eng 2015;102(3-4): 766-783.
14. Ma ZH, Qian L, Martinez-Ferrer PJ et al. An overset mesh based multiphase flow solver for water entry problems. Comput Fluids 2018;172: 689-705.
15. Wang Y, Jimack PK, Walkley MA. A one-field monolithic fictitious domain method for fluid-structure interactions. Comput Method Appl M 2017;317: 1146-1168.
16. Kim W, Lee I, Choi H. A weak-coupling immersed boundary method for fluid-structure interaction with low density ratio of solid to fluid. J Comput Phys 2018;359: 296-311.
17. Wang Y, Zhou L, Wu Y, Yang Q. New simple correlation formula for the drag coefficient of calcareous sand particles of highly irregular shape. Powder Technol 2018;326: 379-392.
18. Bagheri G, Bonadonna C. On the drag of freely falling non-spherical particles. Powder Technol 2016;301: 526-544.
19. Koblitz AR, Lovett S, Nikiforakis N, Henshaw WD. Direct numerical simulation of particulate flows with an overset grid method. J Comput Phys 2017;343: 414-431.
20. Shen Z, Wan D, Carrica PM. Dynamic overset grids in openfoam with application to kcs self-propulsion and maneuvering. Ocean Eng 2015;108: 287-306.
21. Rzehak R, Krepper E. Euler-euler simulation of mass-transfer in bubbly flows. Chem Eng Sci 2016;155: 459-468.
22. Zhao L, Mao J, Bai X et al. Finite element simulation of impulse wave generated by landslides using a three-phase model and the conservative level set method. Landslides 2016;13(1): 85-96.
23. Cruchaga M, Battaglia L, Storti M, D'Elia J. Numerical modeling and experimental validation of free surface flow problems. Arch of Comput Method E 2016;23(1): 139-169.
24. Mao J, Zhao L, Liu X, Cheng J, Avital E. A three-phases model for the simulation of landslide-generated waves using the improved conservative level set method. Comput Fluids 2017;159: 243-253.

25. Niethammer M, Brenn G, Marschall H, Bothe D. An extended volume of fluid method and its application to single bubbles rising in a viscoelastic liquid. J Comput Phys 2019;387: 326-355.
26. Orona JD, Zorrilla SE, Peralta JM. Computational fluid dynamics combined with discrete element method and discrete phase model for studying a food hydrofluidization system. Food Bioprod Process 2017;102: 278-288.
27. Padding JT, Deen NG, Peters EAJF, Kuipers JAM, 2015. Chapter three - euler–lagrange modeling of the hydrodynamics of dense multiphase flows. In: G.B. Marin and J. Li (Editors), Advances in chemical engineering. Academic Press, 137-191.
28. Chen Z, Wang HM, Zhuo JK, You CF. Experimental and numerical study on effects of deflectors on flow field distribution and desulfurization efficiency in spray towers. Fuel Process Technol 2017;162: 1-12.
29. Zhou H, Yang Y, Wang L. Numerical investigation of gas-particle flow in the primary air pipe of a low nox swirl burner - the dem-cfd method. Particuology 2015;19: 133-140.
30. Zbib H, Ebrahimi M, Ein-Mozaffari F, Lohi A. Comprehensive analysis of fluid-particle and particle-particle interactions in a liquid-solid fluidized bed via cfd-dem coupling and tomography. Powder Technol 2018;340: 116-130.
31. Zhao L, Liu X, Mao J et al. A novel discrete element method based on the distance potential for arbitrary 2d convex elements. Int J Numer Methods Eng 2018;115(2): 238-267.
32. Zhao JD, Shan T. Coupled cfd-dem simulation of fluid-particle interaction in geomechanics. Powder Technol 2013;239: 248-258.
33. Zhao T, Utili S, Crosta GB. Rockslide and impulse wave modelling in the vajont reservoir by dem-cfd analyses. Rock Mech Rock Eng 2016;49(6): 2437-2456.
34. Wang Y, Zhou L, Yang Q. Hydro-mechanical analysis of calcareous sand with a new shape-dependent fluid-particle drag model integrated into cfd-dem coupling program. Powder Technol 2019;344: 108-120.
35. Cheng K, Wang Y, Yang Q. A semi-resolved cfd-dem model for seepage-induced

fine particle migration in gap-graded soils. Comput Geotech 2018;100: 30-51.
36. Ergun S. Fluid flow through packed columns. Chem Eng Prog 1952;48(2): 89-94.
37. Di Felice R. The voidage function for fluid-particle interaction systems. Int J Multiphase Flow 1994;20(1): 153-159.
38. Sakai M, Yamada Y, Shigeto Y et al. Large-scale discrete element modeling in a fluidized bed. Int J Numer Meth Fl 2010;64(10-12): 1319-1335.
39. Peskin CS. Numerical analysis of blood flow in the heart. J Comput Phys 1977;25(3): 220-252.
40. Ji C, Munjiza A, Williams JJR. A novel iterative direct-forcing immersed boundary method and its finite volume applications. J Comput Phys 2012;231(4): 1797-1821.
41. Munjiza A, The combined finite-discrete element method. Wiley, Chichester, UK, 2004.
42. Fadlun EA, Verzicco R, Orlandi P, Mohd-Yusof J. Combined immersed-boundary finite-difference methods for three-dimensional complex flow simulations. J Comput Phys 2000;161(1): 35-60.
43. Chorin AJ. A numerical method for solving incompressible viscous flow problems (reprinted from the journal of computational physics, vol 2, pg 12-26, 1997). J Comput Phys 1997;135(2): 118-125.
44. Allen M, Tildesley D, Computer simulation of liquids. Oxford University Press,, 1987.
45. Persillon H, Braza M. Physical analysis of the transition to turbulence in the wake of a circular cylinder by three-dimensional navier-stokes simulation. J Fluid Mech 1998;365: 23-88.
46. Liu C, Zheng X, Sung CH. Preconditioned multigrid methods for unsteady incompressible flows. J Comput Phys 1998;139(1): 35-57.
47. Williamson CHK. Oblique and parallel modes of vortex shedding in the wake of a circular cylinder at low reynolds numbers. J Fluid Mech 1989;206: 579-627.
48. Uhlmann M. An immersed boundary method with direct forcing for the simulation of particulate flows. J Comput Phys 2005;209(2): 448-476.

49. Yang J, Stern F. A non-iterative direct forcing immersed boundary method forstrongly-coupled fluid-solid interactions. J Comput Phys 2015;295: 779-804.
50. Blackburn HM, Karniadakts GE, Two- and three-dimensional simulations of vortex-induced vibration of a circular cylinder. Proceedings of the Third (1993) International Offshore and Polar Engineering Conference, 715-720, 1993.
51. Glowinski R, Pan TW, Hesla TI, Joseph DD, Periaux J. A fictitious domain approach to the direct numerical simulation of incompressible viscous flow past moving rigid bodies: Application to particulate flow. J Comput Phys 2001;169(2): 363-426.
52. Lv H, Tang S. Direct numerical simulation of sedimentation of rectangular particle with ale method. Journal of Chongqing University 2010;(06): 83-90.
53. Jafari S, Yamamoto R, Rahnama M. Lattice-boltzmann method combined with smoothed-profile method for particulate suspensions. Phys Rev E 2011;83(2).
54. Wang L, Guo ZL, Mi JC. Drafting, kissing and tumbling process of two particles with different sizes. Comput Fluids 2014;96: 20-34.